

ESD TDR 64-561

ESTI FILE COPY

ESD-TDR-64-561

ESTI PROCESSED

ESD RECORD COPY

RETURN TO
SCIENTIFIC & TECHNICAL INFORMATION DIVISION
(ESTI), BUILDING 1211

COPY NR. _____ OF _____ COPIES

☐ DDC TAB ☐ PROJ OFFICER

☐ ACCESSION MASTER FILE

☐ _____

DATE _____

ESTI CONTROL NR. **AE 44312**

CY NR. 1 OF 1 CVS

3

Solid State Research

1964

Prepared under Electronic Systems Division Contract AF 19 (628)-500 by

Lincoln Laboratory

MASSACHUSETTS INSTITUTE OF TECHNOLOGY

Lexington, Massachusetts



AD609828

The work reported in this document was performed at Lincoln Laboratory, a center for research operated by Massachusetts Institute of Technology, with the support of the U.S. Air Force under Contract AF 19(628)-500.

Non-Lincoln Recipients

PLEASE DO NOT RETURN

Permission is given to destroy this document
when it is no longer needed.

3

Solid State Research

1964

Issued 17 December 1964

Lincoln Laboratory

MASSACHUSETTS INSTITUTE OF TECHNOLOGY

Lexington, Massachusetts



ABSTRACT

This report covers in detail the solid state research work at Lincoln Laboratory for the period 1 July 1964 through 30 September 1964. The topics covered are Solid State Device Research, Laser Research, Materials Research, Band Structure and Spectroscopy of Solids, and Magnetism and Resonance.

Accepted for the Air Force
Stanley J. Wisniewski
Lt Colonel, USAF
Chief, Lincoln Laboratory Office

INTRODUCTION

I. SOLID STATE DEVICE RESEARCH

Laser action in which coherent radiation at 5.2μ emanates from the bulk of the semiconductor has been obtained from InSb n^+pp^+ diodes in which an electron-hole plasma has been established. Below threshold, injection luminescence was obtained from the entire $400\text{-}\mu$ length of the bar-shaped p-type base region to which the n^+ and p^+ contacts had been alloyed. The luminescence results as well as the I-V characteristic of the diodes indicate the formation, under forward bias, of a "large" volume injection plasma in the p-region, as was previously reported for the "madistor." Above threshold, the angular spread of the beam indicates coherent spots of 50μ measured in the direction of the current. This area is about an order of magnitude larger than has been reported for GaAs and InAs lasers. Large, coherently emitting areas mean smaller beam angles, and the large radiating volume is better suited for light amplification, higher output powers, and may possibly lead to lower threshold current densities. Thus many of the limitations of laser action, when it is confined to the junction region, may be eliminated in this, the first diode bulk laser.

Laser action has been obtained in PbSe diodes operated at 12°K . The emitted coherent radiation was at 8.5μ . Thus the wavelength range for diode laser action has been extended beyond the previously reported limit of 6.5μ for PbTe into the 8- to $14\text{-}\mu$ "atmospheric window."

Laser action has been obtained in GaAs at liquid helium temperature by generating electron-hole pairs with a beam of 50-keV electrons. The threshold beam current density was about 1 amp/cm^2 (beam diameter $\sim 0.5\text{ mm}$). Assuming that the mean total energy required to produce a pair in GaAs is 5 eV, and neglecting any backscattering of the 50-keV electron beam, this is equivalent to a threshold current density of 10^4 amp/cm^2 in a diode laser. Backscattering of the beam may reduce this value by as much as 50 percent. "Snooperscope" observation of the sample emission indicates that laser action occurs in filaments along the surface on which the electron beam impinges. The beam diameter, although larger than the 0.21-mm distance between the faces of the Fabry-Perot cavity, was smaller than the 1-mm width in the direction perpendicular to the cavity. By sweeping the beam along this width, different filaments have been preferentially excited. The technique of electron-beam pumping will hopefully permit laser action to be obtained in the visible in those wide-bandgap semiconductors in which it is difficult to produce good p-n junctions or in which resistivities are so high that series resistance and consequent heating preclude the use of electrical injection.

A miniature pulsed-laser-diode transmitter has been mounted inside a small copper cylinder $\frac{1}{2}$ inch in diameter and 1 inch long. This transmitter, which consists of a GaAs diode laser, a capacitor, a charging resistor, and a pnpn switching transistor has successfully operated at room temperature with $1\frac{1}{2}$ watts of peak power output for a pulse length of 20 nsec. Miniature versions of the requisite power supply and low-power trigger source are now being fabricated,

and the complete transmitter should be much smaller than a two-cell flashlight. This room-temperature pulsed-laser system should have many applications in radar and other range-finding equipment.

Single-crystal $(\text{In}_x\text{Ga}_{1-x})\text{As}$ has been grown by a vapor phase reaction, and diodes have been fabricated from these crystals which lased within the $8750 \pm 50\text{-}\text{\AA}$ range required to pump a Nd^{+3} laser efficiently. In addition, the crystal quality has been improved so that the threshold current densities are now typically 3000 amp/cm^2 at 77°K , and the power output from these mixed-crystal diodes is essentially the same as that from good GaAs diode lasers.

In order to observe the pattern of infrared radiation from the surface of a diode laser, a sensitive scanning infrared microscope has been constructed. This image converter, which uses a slow mechanical mirror scanning system in conjunction with an InSb photodetector, is able to display, on an oscilloscope, images of sources emitting radiation of wavelengths from the visible to 5.4μ . Potentiometers mechanically linked to the mirror position yield voltage to drive the x- and y-axes of an oscilloscope, and the output signal from the photodetector suitably amplified by a phase-sensitive amplifier is used to modulate the intensity of the oscilloscope trace. A magnification of about 25 times with a resolution of about 40μ has been achieved for this scanning microscope system.

Inversion of the $\{111\}$ surface occurs in single-crystal regrowth during interface alloying of intermetallic compounds, if A $\{111\}$ surfaces are mated to A $\{111\}$ surfaces or B $\{111\}$ surfaces are mated to B $\{111\}$ surfaces. Since A $\{111\}$ surfaces develop etch pits in oxidizing etchants whereas B $\{111\}$ surfaces do not, we have used etching studies to detect this diatomic inversion in the recrystallized region of the lower-melting-point semiconductor with respect to the unmelted portion of this semiconductor. The results indicate that the recrystallized region grows as a single crystal which emanates from the surface of the higher-melting-point semiconductor.

The Gunn effect oscillator has been operated CW. All such oscillators have previously operated only on a pulsed basis ($\sim 1\text{-}\mu\text{sec}$ pulses) to prevent overheating and burnout of the devices. By careful heat-sinking of a $25\text{-}\mu$ thick, $125\text{-}\mu$ square, 1-ohm-cm GaAs, continuous room-temperature operation was possible with the output predominantly at 5 Gcps but with substantial output at many other frequencies. The 5-Gcps frequency is predicted from the equation originally presented by Gunn. It is now necessary to terminate the oscillator with the proper impedance network so that single-frequency operation can be obtained.

11. LASER RESEARCH

Stimulated Raman emission at 90° to the ruby-laser beam in CS_2 has been obtained, and the threshold has been compared with that in nitrobenzene. With mirrors that reflect ruby-laser wavelengths placed in the Raman cavity (filled with CS_2 or nitrobenzene), a narrow laser-like beam at $6943\text{ }\text{\AA}$ radiates at 90° to the primary laser beam. Presently, etalon photographs are being taken to establish that this is a 90° Brillouin laser, down-shifted by 4.25 Gcps from the pump frequency.

Effects of enhancement of stimulated Raman emission by a cavity set at angles other than 0° and 90° to the ruby-laser direction have been observed. The intensity of the anti-Stokes radiation AS_1 still peaks at the usual phase-matching angle but is optimized when the cavity angle is at the phase-matching angle for S_1 .

For a variety of solids and liquids, data have been obtained on the number of stimulated Stokes, anti-Stokes, and multiple-scattering lines that are achievable with a particular ruby laser.

A study has been made of the time, pressure, and wavelength characteristics of the afterglow in a ruby-laser-created breakdown in several gases. Volume electron-ion recombination, and not diffusion, appears to be the dominant loss mechanism of electrons in argon and hydrogen. An argon-afterglow electron temperature of about 5300°K was estimated from the ratio of spectral line intensities, and the electron density of $2.5 \times 10^{18} \text{ cm}^{-3}$ was measured from Stark-broadened line widths. There is only a small pressure dependence of the characteristic time of decay of the afterglow.

Perturbation of the refractive index of absorbing media due to the propagation of a $1.06\text{-}\mu$ glass laser has been observed in a Mach-Zehnder interferometer. The observed changes of index are consistent with the estimated energy deposition, the known temperature coefficient of the index, and the heat capacity of each medium. The interferometer is illuminated by a very short pulse from an argon laser at varying times after the start of the long-duration glass-laser emission. The index changes in the gas deviated the interferometer rays by almost a milliradian, and the considerable turbulence in the liquid obliterated the interference fringes.

III. MATERIALS RESEARCH

An electric furnace has been developed for heating samples to 2400°C in oxidizing atmospheres, as well as in neutral or reducing atmospheres. The furnace employs a tantalum split-tube heating element, operated in argon, which is isolated from the sample and sample atmosphere by an inner tube of dense zirconia. It has been used successfully for Czochralski growth of sapphire crystals and should also find application in such areas as phase studies, material testing, and diffusion experiments.

Measurements of the Seebeck coefficient and resistivity of polycrystalline CrO_2 prepared by high-pressure synthesis have been extended to liquid helium temperature for samples with compositions of $\text{CrO}_{1.994}$ and $\text{CrO}_{2.015}$. The stoichiometry of these and other samples was measured by an analytical method which determines the chromium content to an accuracy of about 1 part per 1000. The electrical properties of samples with compositions between $\text{CrO}_{1.89}$ and $\text{CrO}_{2.02}$ are similar, as expected on the basis of the Goodenough model used to explain the metallic properties and ferromagnetism of CrO_2 .

The phase diagram for the pseudo-binary InSb-InTe system has been determined by thermal, x-ray, and metallographic analysis. The system contains a peritectic compound, In_4SbTe_3 .

(rock-salt structure), which forms a eutectic with InSb. In_4SbTe_3 is the primary phase that crystallizes from the melt between the eutectic point (15 mol % InTe, 508°C) and the peritectic point (40 mol % InTe, 556°C). InTe is the primary stable phase that crystallizes from melts containing more than 40 mol % InTe, but the primary crystallization of In_4SbTe_3 as an unstable phase has been observed for melts containing between 40 and 75 mol % InTe.

Samples of In_4SbTe_3 prepared at atmospheric pressure or below do not exhibit superconductivity down to 1.3°K, the lowest temperature investigated. Samples prepared at high pressure (37 kbar) become superconducting at about 1.5°K, although x-ray diffraction measurements indicate no difference in structure or lattice constant between the low- and high-pressure forms.

Superconductivity measurements have been made on InSb_{11} - β -Sn alloy samples annealed under pressure (37 kbar) for 20 to 40 hours. Each sample, regardless of composition, exhibits only one superconducting transition, whereas in earlier experiments transitions at two different temperatures were observed in samples containing 0.2 to 0.4 atom-fraction tin which had been annealed for only one hour under pressure. It is concluded that InSb_{11} and β -Sn, which have the same tetragonal structure, form solid solutions in all proportions, if sufficient time is allowed for equilibrium to be reached. The superconducting transition temperature has a maximum value of about 5°K at 0.5 atom-fraction tin, compared with transition temperatures of 2.1° and 3.7°K for InSb_{11} and β -Sn, respectively.

IV. BAND STRUCTURE AND SPECTROSCOPY OF SOLIDS

The experimental investigation of the energy bands in antimony is continuing. Two new sets of oscillations have been observed in the magnetorefectivity. In contrast to the previously observed deHaas-Shubnikov magneto-oscillations for which the magnetic field associated with a particular oscillation is independent of photon energy, the present phenomenon is strongly frequency dependent and is associated with interband transitions across two different energy gaps. The oscillations are more readily observed when appropriately polarized light is used for the various crystallographic directions. It is believed that these interband transitions can resolve some puzzling features of earlier measurements on the magnetoplasma and optical deHaas-Shubnikov effects.

By using the energy band parameters in graphite obtained from the magnetoreflexion experiments, the magnetic susceptibility and microwave transmission in graphite are being calculated. So far, calculations of cross-sectional areas of the Fermi surface indicate that the Slonczewski-Weiss model is capable of predicting all the observed periods, including the long-period oscillations recently observed by Soule. Calculations of the microwave transmission yield both Alfvén wave and cyclotron resonance behavior.

Previous measurements of the ultraviolet reflectivity of Mg_2Ge have now been complemented with similar measurements in Mg_2Si and Mg_2Sn . The structure in the reflectivity of these II-IV compounds is very similar to materials of the zinc-blende structure. A Kramers-Krönig

analysis on the data is presently under way in order to facilitate interpretation in terms of published band-structure calculations.

On the basis of optical, magneto-optical, and transport experiments and theoretical arguments involving symmetry and continuity, a model has been proposed for the band structure of HgTe and $\text{Cd}_x\text{Hg}_{1-x}\text{Te}$ alloys. This model, which is similar to that in gray tin proposed by Groves and Paul except that it includes overlap of the valence and conduction bands, is consistent with the systematics of III-V and II-VI compounds and all available experimental data.

In collaboration with the M.I.T. National Magnet Laboratory and Bell Telephone Laboratories personnel, the nonrelativistic energy bands in gadolinium metal are being calculated. Initial results of the augmented plane-wave calculation indicate marked differences from a free-electron model and, in fact, indicate some similarity to the situation in transition metals.

Work on transport problems is continuing. A more general theory of the "collision drag" effect on the ultrasonic absorption in metals has been developed. The theoretical description is based on a transport theory for inhomogeneous driving fields which had been developed previously. The collision drag effect has been treated only for special cases.

A formal and systematic treatment of the elastotransport phenomena in one-carrier semiconductors and metals has been completed. Explicit formulas for the piezoeffects due to the electrons have been developed which take into account not only the deformation potential effects, but also the effects of strain on the effective mass tensors, intravalley scattering, and the Fermi level. The formulas are developed in terms of the Fermi-Dirac statistics.

The elastic constants of HgTe have been measured at room temperature by means of the ultrasonic pulse technique. By using the measured values of these constants, a fundamental lattice absorption frequency ω_0 , which is in reasonable agreement with far infrared measurements, and a Debye characteristic temperature at absolute zero, $\Theta_0 = 105^\circ\text{K}$, have been calculated.

A theoretical and experimental study has been made of wave transmission through degenerate hole-electron plasmas, emphasizing weakly transmitted waves which have not previously been examined in detail. Two of these waves, the resonance-damped Alfvén wave and the so-called "branch cut" wave (which is a superposition of single-particle excitations), were studied in bismuth at 4.2°K as a function of magnetic field. At zero magnetic field, the transmitted wave has a phase and group velocity of about 7×10^7 cm/sec and appears to be due to electron single-particle excitations.

V. MAGNETISM AND RESONANCE

A new high-temperature expansion has been developed which permits calculation of the Curie temperature T_c and provides new insights into the form of the magnetic ordering in the neighborhood of this temperature. It is hoped that this type of investigation will not only provide independent quantitative checks for any exchange-energy formalism, but will also show how to handle the disorder in the spiral components that have been observed below T_c in CoCr_2O_4 .

Spin resonance can provide important independent information about spin configurations below T_c and is therefore being used to study several chromium spinels. At low temperatures, the spin resonance in $MnCr_2O_4$ and $MnCr_2S_4$ shows satellite structure on the uniform mode resonance. The uniform mode resonance in $CoCr_2S_4$ splits into two resonances at low temperature. It is not yet clear whether the structures observed are related to other modes of the system or are due to powder samples that cause averaging over the anisotropies of the crystals.

Investigation of the breakdown of ligand-field theory has been extended to the thiospinels. It is shown that a consistent interpretation of their magnetic and electric properties requires the assumption that cationic d-orbitals directed toward nearest-neighbor ligands are transformed via cation-anion covalence into antibonding σ^* -bands. The only exceptions to this generalization may occur when there are four or five unpaired spins per cation.

In order to obtain materials for the investigation of transport properties, work on methods of growing chemically controlled single crystals continues. Vanadium spinels are being grown from fluxes by electrolytic reduction, ReO_3 has been grown by vapor deposition, and suitable fluxes for the growth of YAG and $InVO_4$ host crystals are being investigated.

Several of the rare-earth trifluorides have been prepared and their magnetic susceptibilities have been studied from 4° to 300°K. The materials are characterized by small Weiss constants Θ and values of μ_{eff} close to those expected for free rare-earth ions.

Studies of the effect of Mn^{3+} on the crystal chemistry of lithium spinels have continued. Crystallographic evidence has been obtained to support the idea that, at the critical concentration of Mn^{3+} for the destruction of long-range ordering of Li^+ on the B-sites, there is also a discontinuous change in the distribution of Li^+ ions over the A- and B-sites.

TABLE OF CONTENTS

Abstract	ii
Introduction	iii
Organization	xi
Reports by Authors Engaged in Solid State Research	xii
 I. SOLID STATE DEVICE RESEARCH	 1
A. Luminescence and Coherent Emission in a Large-Volume Injection Plasma in InSb	1
B. PbSe Diode Laser	3
C. Electron-Beam-Pumped GaAs Laser	5
D. Room-Temperature GaAs Pulsed-Laser Transmitter	7
E. Scanning Infrared Microscope	9
F. Inversion of {111} Surfaces in Single-Crystal Regrowth During Interface Alloying of Intermetallic Compounds	11
G. CW Gunn Effect Oscillator	13
H. Growth of $(\text{In}_x\text{Ga}_{1-x})\text{As}$ Single Crystals by Vapor Phase Reaction	14
 II. LASER RESEARCH	 17
A. Raman Laser Program	17
1. Stimulated Raman Emission at 90° to the Ruby-Laser Beam	17
2. Enhancement of Stimulated Raman Scattering by an Off-Axis Cavity	17
3. Stimulated Raman Emission	19
4. Experiments to Convert Stimulated Raman Excitation into Infrared Radiation	19
B. Gaseous Discharge Produced by a Giant-Pulsed Ruby Laser	19
1. Argon	21
2. Hydrogen	24
C. Perturbation of the Refractive Index of an Absorbing Medium by a Laser Beam	25
 III. MATERIALS RESEARCH	 29
A. Electric Furnace for Operation in Oxidizing, Neutral, and Reducing Atmospheres to 2400°C	29
B. Electrical Properties of CrO_2	31
C. InSb-InTe System	33
1. Phase Diagram	33
2. Superconductivity	35
D. Superconductivity in the High-Pressure InSb - β -Sn System	36

IV. BAND STRUCTURE AND SPECTROSCOPY OF SOLIDS	39
A. Interband Transitions in Antimony	39
B. Magnetic Susceptibility in Graphite	40
C. Alfvén Waves in Graphite	40
D. Reflectivity of Mg_2Si , Mg_2Ge , and Mg_2Sn	41
E. Band Structure of HgTe and HgTe-CdTe Alloys	41
F. Band Structure of Gadolinium Metal	45
G. Theory of the "Collision Drag" Effect in Ultrasonic Absorption in Metals	45
H. Elastotransport Properties of Materials	46
I. Elastic Constants of HgTe	46
J. Plasma Wave Transmission Through Bismuth	46
V. MAGNETISM AND RESONANCE	51
A. Magnetic Ordering	51
1. On the Determination of Magnetic Ordering from High-Temperature Expansions	51
2. Ferrimagnetic Resonance in Chromium Spinels	51
B. Modification of Ligand-Field Theory for Thiospinels	52
C. Single-Crystal Growth	52
1. Vanadium Spinels	53
2. Rhenium Trioxide	53
3. Yttrium Aluminum Garnet and Indium Vanadate	54
D. Preparation and Susceptibility of Rare-Earth Trifluorides and Oxyfluorides	54
E. Effect of Mn^{+3} on the Crystal Chemistry of Some Lithium Spinels	54

ORGANIZATION

SOLID STATE DIVISION

A. L. McWhorter, *Acting Head*
 P. E. Tannenwald, *Assistant Head*
 M. J. Hudson, *Assistant*
 D. T. Stevenson*
 R. H. Kingston†

GROUP 81

SEMICONDUCTOR PHYSICS

J. M. Honig, *Leader*
 T. C. Harman, *Assistant Leader*

Argyres, P. N.	Kelley, P. L.
Brebrick, R. F.	Kleiner, W. H.
Dresselhaus, G. F.	Mason, V. J.
Duston, D. K.‡	Paladino, A. E.
Gardner, M.	Rawson, N. B.*
Groves, S. H.	Sigel, J. L.§
Hilsenrath, S.	Trent, P. H.
Houghton, B. H.*	Van Zandt, L. L.
Jones, L. M.§	Work, C. C.

GROUP 83

ELECTRONIC MATERIALS

E. P. Warekois, *Leader*
 A. J. Strauss, *Assistant Leader*

Andrews, H. I.‡	Giardino, N. A.
Bachner, F. J.‡	Kafalas, J. A.
Banus, M. D.	LaFleur, W. J.
Button, M. J.	Lavine, M. C.*
Carter, F. B.	Owens, E. B.
Cornwell, J. C.	Plonko, M. C.
Ehlers, H. H.	Reed, T. B.
Fahey, R. E.	Roddy, J. T.
Farrell, L. B.	Siuta, V. P.‡
Finn, M. C.	Vernon, S. N.‡
Fischler, S.	

GROUP 85

APPLIED PHYSICS

R. H. Rediker, *Leader*
 R. J. Keyes, *Assistant Leader*

Bates, D. H.	May, W. G.‡
Berninger, W. H.§	Melngailis, I.
Butler, J. F.	Palermo, J. S.
Calawa, A. R.	Phelan, R. J., Jr.
Caswell, F. H.	Quist, T. M.
Clough, T. F.	Stopek, S.
Donaldson, P. L.	Sullivan, F. M.
Foyt, A. G.¶	Walpole, J. M.‡
Grant, C. R.	Ward, J. H. R., III
Hinkley, E. D.	Youtz, P.
Hurwitz, C. E.	

GROUP 82

MAGNETISM AND RESONANCE

J. B. Goodenough, *Leader*
 H. J. Zeiger, *Associate Leader*

Arnott, R. J.	Menyuk, N.
Bermon, S.	Newman, W. A.
Burke, J. W.	Parker, C. D.
Delaney, E. J.	Perry, F. H.
Dwight, K., Jr.	Raccach, P. M.
Feinleib, J.	Ridgley, D. H.
Feldman, B.	Rogers, D. B.
Ferretti, A.	Stanley, H. E.§
Germann, R. W.	Stickler, J. J.
Kaplan, T. A.	Thaxter, J. B.
Kern, S.	Weber, R.
Kernan, W. C.	Weinberg, D. L.
Maltz, M. S.§	Whipple, E. R.

GROUP 84

SOLID STATE SPECTROSCOPY

J. G. Mavroides, *Leader*
 G. B. Wright, *Assistant Leader*

Carman, R. L.§	Johnson, E. J.
Curran, E. A.	Kolesar, D. F.
Dickey, D. H.	Krag, W. E.
Dimmock, J. O.	Larsen, D. M.
Dresselhaus, M. S.	Mason, W. C.
Edwards, D. F.	Mastromattei, E. L.
Fulton, M. J.	Scouler, W. J.
Halpern, J.	Strahm, N. D.§

GROUP 86

OPTICS AND INFRARED

F. L. McNamara, *Acting Leader*
 M. M. Litvak, *Assistant Leader*

Billups, R. R.	Merrill, E. R.
Bostick, H. A.	O'Connor, J. R.
Carbone, R. J.	Pitts, R. F.
Chatterton, E. J., Jr.	Rotstein, J.
Dennis, J. H.	Schlickman, J. J.
DiMarzio, E. W.	Soref, R. A.
Eisenberger, P. M.§	Underwood, D. I.
Fitzgerald, M. E.§	Wong, G. W.
Freed, C.	Ziegler, H. L.
Kuppenheimer, J. D., Jr.§	Zieman, H. E.
Longaker, P. R.	Zimmerman, M. D.

*Part Time

§Summer Staff

†Leave of Absence

¶Staff Associate

‡Research Assistant

REPORTS BY AUTHORS ENGAGED IN SOLID STATE RESEARCH

15 July through 15 October 1964

PUBLISHED REPORTS

Journal Articles*

JA No.

2136	Magnetic Properties of a Single Crystal of Manganese Phosphide	E. E. Huber, Jr. [†] D. H. Ridgley	Phys. Rev. <u>135</u> , A1033 (1964)
2194	Magnetoreflexion Experiments in Graphite	M. S. Dresselhaus J. G. Mavroides	Carbon <u>1</u> , 263 (1964)
2271	Classical Ground Spin Configurations in the Corundum Lattice	N. Menyuk K. Dwight	J. Phys. Chem. Solids <u>25</u> , 1031 (1964)
2272	A Cluster Method for Finding Minimum Energy Spin States	D. H. Lyons [‡] T. A. Kaplan	J. Phys. Chem. Solids <u>25</u> , 645 (1964)
2295	Interface-Alloy Epitaxial Heterojunctions	R. H. Rediker S. Stopek J. H. R. Ward	Solid-State Electron. <u>7</u> , 621 (1964)
2305	Diffused Junction Diodes of PbSe and PbTe	J. F. Butler	J. Electrochem. Soc. <u>111</u> , 1150 (1964)
2332	Partial Pressures in Equilibrium with Group IV Tellurides. III. Germanium Telluride	R. F. Brebrick	J. Chem. Phys. <u>41</u> , 1140 (1964)
2335	Band Edge Structure of PbS, PbSe, and PbTe	J. O. Dimmock G. B. Wright	Phys. Rev. <u>135</u> , A821 (1964)
2344	Galvano-Thermomagnetic Effects in Semiconductors and Semimetals. IV. Mercury Selenide	T. C. Harman	J. Phys. Chem. Solids <u>25</u> , 931 (1964)
2359	Acoustic Plasma Waves in Semimetals	A. L. McWhorter W. G. May	IBM J. Research Develop. <u>8</u> , 285 (1964)
2361A	Energy Levels of d ¹ Electrons in CaF ₂ . Evidence of Strong Dynamical Jahn-Teller Distortions	J. R. O'Connor J. H. Chen [‡]	Appl. Phys. Letters <u>5</u> , 100 (1964)

* Reprints available.

[†] Division 2.

[‡] Author not at Lincoln Laboratory.

Published Journal Articles (Continued)

JA No.

- | | | | |
|------|---|---|---|
| 2384 | Efficiency in a Tetrahedral-Anvil Press as Related to Anvil and Pyrophyllite Size | M. D. Banus
S. D. Nye | Rev. Sci. Instr. <u>35</u> , 1319 (1964) |
| 2389 | Reststrahlen Reflection in HgTe | D. H. Dickey
J. G. Mavroides | Solid State Commun. <u>2</u> , 213 (1964) |
| 2391 | Stimulated Raman Emission at 90° to the Ruby Beam | J. H. Dennis
P. E. Tannenwald | Appl. Phys. Letters <u>5</u> , 58 (1964) |
| 2398 | Temperature Dependence of Attenuation of 70-Gc/sec Acoustic Waves in Quartz | J. B. Thaxter
P. E. Tannenwald | Appl. Phys. Letters <u>5</u> , 67 (1964) |
| 2405 | PbTe Diode Laser | J. F. Butler
A. R. Calawa
R. J. Phelan, Jr.
T. C. Harman
A. J. Strauss
R. H. Rediker | Appl. Phys. Letters <u>5</u> , 75 (1964) |
| 2416 | Luminescence and Coherent Emission in a Large-Volume Injection Plasma in InSb | I. Melngailis
R. J. Phelan, Jr.
R. H. Rediker | Appl. Phys. Letters <u>5</u> , 99 (1964) |
| 2417 | Inversion of {111} Surfaces in Single Crystal Regrowth During Interface-Alloying of Intermetallic Compounds | E. D. Hinkley
R. H. Rediker
M. C. Lavine | Appl. Phys. Letters <u>5</u> , 110 (1964) |
| 2419 | PbSe Diode Laser | J. F. Butler
A. R. Calawa
R. J. Phelan, Jr.
A. J. Strauss
R. H. Rediker | Solid State Commun. <u>2</u> , 301 (1964) |
| 2436 | Distribution of Magnetic Moment in Hexagonal Cobalt | R. M. Moon | Phys. Rev. <u>136</u> , A195 (1964) |
| 2437 | Electron-Beam-Pumped GaAs Laser | C. E. Hurwitz
R. J. Keyes | Appl. Phys. Letters <u>5</u> , 139 (1964) |

MS No.

- | | | | |
|-----|---|--|--|
| 787 | Electrical Properties of Praseodymium Oxides | J. M. Honig
A. A. Cella
J. C. Cornwell | } Proc. Third Rare Earth Conference, Clearwater, Florida, 21-24 April 1963 |
| 835 | Praseodymium - Group V Compounds. I. Vaporization Behavior and Nonstoichiometry of PrP, PrAs, PrSb and PrBi | K. A. Gingerich* | |

* Author not at Lincoln Laboratory.

Published Journal Articles (Continued)

MS No.			
925	Ferrimagnetic Spiral Configurations in Cobalt Chromite	N. Menyuk K. Dwight A. Wold	J. de Physique <u>25</u> , 528 (1964)
940	Narrow Band vs Localized d Electrons	J. B. Goodenough	Proc. Buhl International Conference on Materials, Pittsburgh, Pennsylvania, 31 October - 1 November 1963
968	The Fermi Surface of Graphite	M. S. Dresselhaus J. G. Mavroides	IBM J. Research Develop. <u>8</u> , 262 (1964)

UNPUBLISHED REPORTS

JA No.		<u>Journal Articles</u>	
2374	Aspherical Spin-Density in S-State Cations	T. A. Kaplan	Accepted by Phys. Rev.
2380A	Optical deHaas-Shubnikov Effect in Antimony	M. S. Dresselhaus J. G. Mavroides	Accepted by Solid State Commun.
2390	Electrochemical Demer Effect in Semiconductors	W. W. Harvey* M. C. Finn	Accepted by Surface Sci.
2392	Single Crystal Growth of Transition Metal Oxides	W. Kunmann A. Ferretti R. J. Arnott D. B. Rogers	Accepted by J. Phys. Chem. Solids
2394	The Band Gap of Boron Phosphide	R. I. Stearns*	Accepted by J. Appl. Phys.
2412	Peritectic Reaction in the Superconductor Nb ₃ Sn	F. J. Bachner H. C. Gatos M. D. Banus	Accepted by Metallurgical Trans., AIME
2413A	Band Structure of HgTe and HgTe-CdTe Alloys	T. C. Harman W. H. Kleiner A. J. Strauss G. B. Wright J. G. Mavroides J. M. Honig D. H. Dickey	Accepted by Solid State Commun.
2418	Semiconductor Injection Laser	R. H. Rediker	Accepted by 1965 McGraw-Hill Yearbook of Science and Technology
2446	Electromagnetic Mode Mixing in Nonlinear Media	R. H. Kingston A. L. McWhorter	Accepted by Proc. IEEE
2452	Elastic Constants of HgTe	J. G. Mavroides D. F. Kolesar	Accepted by Solid State Commun.

* Author not at Lincoln Laboratory.

Unpublished Journal Articles (Continued)

MS No.

989	The Phase Transition Region of $\text{PrO}_{1.5}$	D. S. Chapin M. C. Finn J. M. Honig	Accepted by Proc. Fourth Rare Earth Conference, Phoenix, Arizona, 22-25 April 1964
1002	Galvano-Thermomagnetic Phenomena in Bismuth	T. C. Harman J. M. Honig B. M. Tarmy	Accepted by Proc. 1964 International Conference on Physics of Semiconductors, Paris, 19-24 July 1964
1131	Electrical Properties of Interface-Alloyed Heterojunctions	R. H. Rediker S. Stopek E. D. Hinkley	Accepted by Metallurgical Trans., AIME

Meeting Speeches*

MS No.

983B	Stoichiometry of Electronic Materials	A. J. Strauss	Seminar, Sprague Electric Company, North Adams, Massachusetts, 18 September 1964
1009	Magnetic Properties of V^{3+} Ions in Cubic Spinels	K. Dwight N. Menyuk D. B. Rogers A. Wold	1964 International Conference on Magnetism, Nottingham, England, 7-11 September 1964
1014	Spin Quenching in the System $\text{MnAs}_{1-x}\text{P}_x$ and $\text{MnAs}_{1-y}\text{Sb}_y$	J. B. Goodenough D. H. Ridgley W. A. Newman	
1010A	On the Symmetry of Spin Configurations in Magnetic Crystals	J. O. Dimmock	Sagamore Conference on Charge and Spin Density, Sagamore, New York, 18-21 August 1964
1011	Injection Luminescence in InAs Diodes	I. Melngailis	Symposium on Radiative Recombination in Semiconductors, Paris, 27-28 July 1964
1013	Injection Luminescence and Laser Action in InSb	R. J. Phelan, Jr. R. H. Rediker	
1034	The Mass Spectrographic Analysis of Powdered Samples	E. B. Owens	ASTM Mass Spectrometry Conference, Paris, 14-18 September 1964
1071	Theory and Measurements of Intensity Fluctuations in Optical Masers	C. Freed H. A. Haus†	Fifth Congress International "Tubes pour Hyperfréquences," Paris, 14-18 September 1964
1116	Transition-Metal Oxides with Metallic Conductivity	J. B. Goodenough	Symposium on the Oxy-Compounds of Transition Elements in the Solid State, Bordeaux, France, 24-27 September 1964

* Titles of Meeting Speeches are listed for information only. No copies are available for distribution.

† Author not at Lincoln Laboratory.

Meeting Speeches (Continued)

MS No.			
1117	The Effect of Trivalent Manganese on Ordering in Lithium Spinels	R. J. Arnott D. B. Rogers R. W. Germann	American Crystallographic Association, Bozeman, Montana, 26-31 July 1964
1139	Thermoelectric Properties of Ferromagnetic CrO_2	D. S. Chapin J. A. Kafalas J. M. Honig	American Chemical Society, Chicago, Illinois, 30 August - 4 September 1964
1146	Magneto-Optics	G. B. Wright	Conference on Undergraduate Research in Optical Physics, Southwestern College, Memphis, Tennessee, 10 June 1964
1154	Properties, Generation and Uses of Plasmas at Thermal Equilibrium	T. B. Reed	Gordon Research Conference, Tilton, New Hampshire, 27-31 July 1964
1162	On the Possibility of Producing Stimulated Emission in Optically-Excited GaAs	J. J. Schlickman M. E. Fitzgerald L. J. Coyne R. H. Kingston	Boston Laser Conference, Northeastern University, 5-7 August 1964
1166	Review of Laser Diodes	T. M. Quist	
1178	High Pressure Phenomena in Some Compound Semiconductors	M. D. Banus	Gordon Research Conference, Tilton, New Hampshire, 28 August 1964
1179	Metallurgical Aspects of GaAs-Ge Heterojunctions	R. S. Mroczkowski* M. C. Lavine H. C. Gatos	AIIME Electronic Materials Conference, Boston, 31 August - 4 September 1964
1181	Junction Injection Luminescence in Semiconductors	R. H. Rediker	Gordon Research Conference, Tilton, New Hampshire, 25 August 1964
1182	Band Structure of HgTe, CdTe-HgTe Alloys and Related Materials	T. C. Harman	Solid State Seminar, RCA Laboratories, Princeton, New Jersey, 24 September 1964
1185	Generation of Stokes and Anti-Stokes Radiation in Raman Media	H. J. Zeiger	Nonlinear Optics Session, Gordon Conference, Meriden, New Hampshire, 31 August - 4 September 1964
1196	deHaas-vanAlphen Effect in Pyrolytic and Single Crystal Graphite	S. J. Williamson* S. Foner* M. S. Dresselhaus	Ninth International Conference on Low Temperature Physics, Columbus, Ohio, 31 August - 4 September 1964
1199	Semiconductor Devices	R. H. Rediker	Electrical Industries Association Symposium, Bedford, Massachusetts, 23 September 1964

* Author not at Lincoln Laboratory.

I. SOLID STATE DEVICE RESEARCH

A. LUMINESCENCE AND COHERENT EMISSION IN A LARGE-VOLUME INJECTION PLASMA IN InSb

Diode injection lasers have been made from several direct-gap semiconductors. In the lasers for which estimates of the size of the active region have been reported,^{1,2} the radiation originates from a very thin sheet of a few microns in or near the transition region of the p-n junction because carrier lifetimes are very short.

We have obtained injection luminescence at wavelengths near 5μ from the entire length of a bar-shaped p-type base region about 400μ long in an n^+pp^+ InSb structure with alloyed contacts. Coherent emission was observed in parts of the injection plasma in structures with opposite sides cleaved to form a laser cavity. The angular spread of the beam indicates coherent spots of 50μ measured in the direction of the current. This is about an order of magnitude larger than has been reported for GaAs (Ref. 1) and InAs (Ref. 2) lasers. The possibility of obtaining large coherently emitting areas implies smaller beam angles, and the large radiating volume is better suited for light amplification.

The formation of a large-volume injection plasma in forward-biased n^+pp^+ InSb structures has been noted previously and has been used in magnetic switching and amplification devices called madistors.³ In these devices, a forward bias injects carriers into the base, which gradually saturate traps and bring about a large increase of carrier lifetime from about 10^{-10} to 10^{-7} to 10^{-6} sec, thus making large-volume injection possible. The saturation of traps in the base manifests itself in a negative-resistance region in the voltage-current characteristic of the structure. Negative-resistance characteristics of related origin have been found in other materials,⁴ and spontaneous emission has been observed in doubly diffused pp^0n GaAs diodes from a 30- to $40\text{-}\mu$ wide p^0 region.⁵

The InSb diodes were made from a p-type crystal with a resistivity of 10 ohm-cm ($N_A - N_D = 6 \times 10^{13} \text{ cm}^{-3}$) at 77°K. An alloy of indium with a small percent of tellurium was used for the n^+ contact. The device was alloyed with one contact to a copper heat sink in a microwave package.

All measurements were made with the diode at about 10°K. As noted earlier in diffused p^+n diodes at 2°K (Ref. 6), magnetic fields applied parallel to the current flow increased the radiation efficiency. Radiation patterns at the diode were observed by means of a mechanical scanning system used in conjunction with an infrared lens and an InSb photovoltaic detector. Figure I-1(a) shows an oscilloscope display of the pattern at a current density of 100 amp/cm^2 in a longitudinal magnetic field of 21 kG. (The negative resistance occurs at about 0.5 amp/cm^2 .) Comparison with the shadow of the diode in Fig. I-1(b) indicates that the radiation is emitted from the entire $400\text{-}\mu$ -long base. Figure I-1(c), taken at zero magnetic field, shows the radiation concentrated near the two contacts. These preliminary results indicate the possibility of using such patterns to study the carrier distribution in semiconductor plasmas.

In a longitudinal magnetic field and with high-current pulses (8000 amp/cm^2), coherently emitting areas were observed near the n^+ contact although the resolution of the image converter

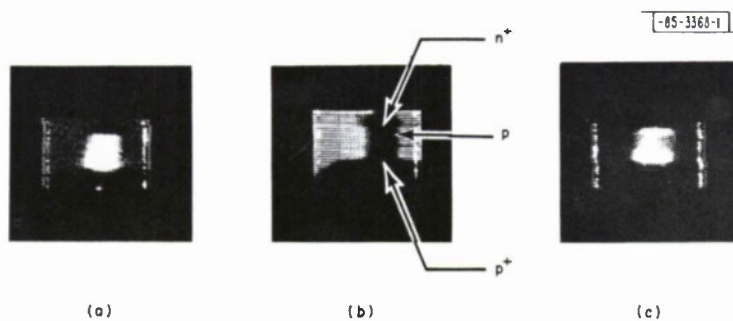


Fig. 1-1. (a) Spontaneous radiation pattern of n^+pp^+ InSb structure with 400- μ -long bar-shaped p-region obtained near 10°K at a 100-ma current and a longitudinal magnetic field of 21 kG. (b) Shadow of diode structure obtained by using visible light. (c) Radiation pattern at 100 mo without magnetic field. Diode cross section was 10^{-3} cm².

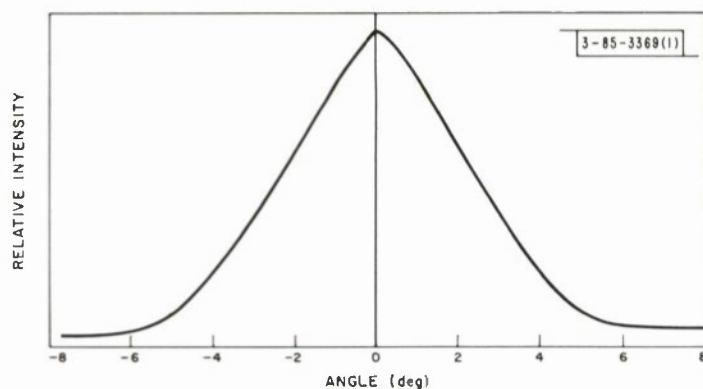


Fig. 1-2. Angular distribution of coherent radiation in a plane perpendicular to the junction plane of n^+pp^+ InSb laser operated near 10°K in a longitudinal magnetic field of 16 kG with 100-nsec-long 16-amp pulses. Laser cross section was 1.4×10^{-3} cm².

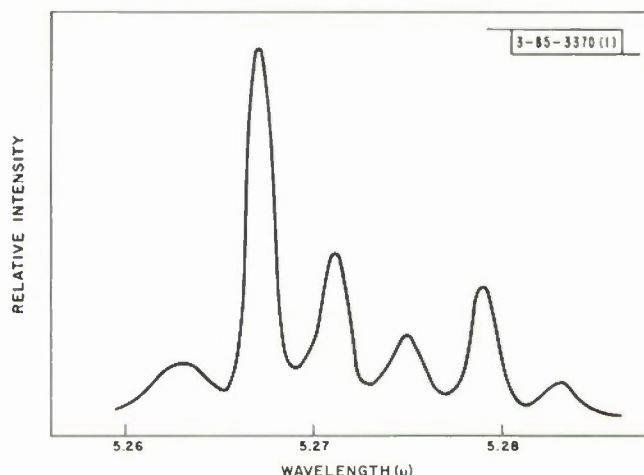


Fig. I-3. Mode structure of the laser of Fig. I-2 operated near 10°K in a field of 16 kG. Amplitude of 100-nsec current pulses was 17 amp.

was insufficient to determine their exact size. The diffraction pattern in most cases consisted of multiple beams, indicating the presence of multiple filaments. Figure I-2 shows one of the simplest beam patterns obtained in the plane perpendicular to the junction at a current just above threshold. A measurement of the spectrum at this current indicated that most of the radiation was in a single cavity mode. The angle at the half-power point is 5.3° , which corresponds to a coherently emitting region of 50μ in the direction of the current; the angle in the junction plane is 8° , which corresponds to 40μ perpendicular to the current. This can be contrasted to other junction lasers^{1,2} in which the coherent spots may extend along the entire junction but measure only a few microns in the direction of the current. The wavelength of the lines (5.22μ at 21 kG) corresponds closely to the wavelength associated with a transition from the lowest energy state of the spin-split lowest Landau level observed in p^+n diffused diodes.^{6,7} Figure I-3 shows mode structure at 16 kG. Radiation was also obtained at a wavelength of 5.085μ at 21 kG, which corresponds to the highest energy state of the Landau level.^{6,7}

I. Melngailis
R. J. Phelan, Jr.
R. H. Rediker

B. PbSe DIODE LASER

Diode laser action has previously been observed in III-V compounds⁸ and in PbTe.⁹ In this section we describe laser action in PbSe diodes,¹⁰ which occurs at 8.5μ and extends the wavelength range for diode laser action beyond the previously reported limit of 6.5μ for PbTe.

The diode lasers were prepared from single-crystal PbSe wafers cleaved from a Bridgman grown ingot. The 1.6-mm-thick n-type wafers were annealed at $659^\circ \pm 1^\circ\text{C}$ for 95 hours under a selenium vapor pressure produced by pure selenium at $211^\circ \pm 1^\circ\text{C}$. In order to reduce sublimation of the wafer, argon at a pressure of 100 torrs was admitted to the system at room temperature before sealing off. The annealed wafers were p-type with hole concentration of $4.7 \times 10^{17} \text{ cm}^{-3}$,

Section I

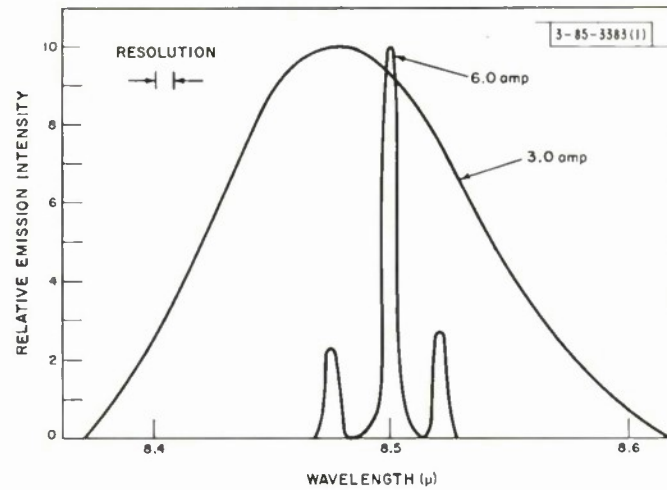


Fig. 1-4. Spectro of infrared emission from cleaved surface of PbSe diode at 12°K below (3.0 amp) and above (6.0 amp) threshold for laser action. Resolution gauge refers to 6-amp spectrum only.

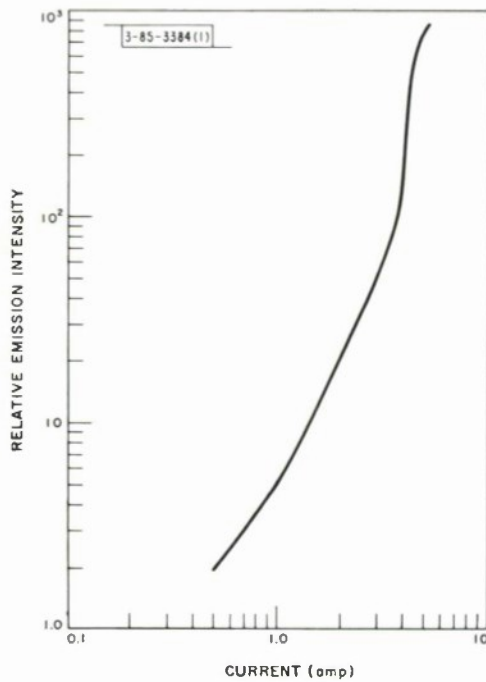


Fig. 1-5. Light emission from cleaved surface of PbSe diode as a function of current at 12°K.

somewhat higher than expected from the results of Igaki and Ohashi,¹¹ and Hall mobility of $3.6 \times 10^4 \text{ cm}^2 \text{ v}^{-1} \text{ sec}^{-1}$ at 77°K. The n-p junction was formed by heating a cleaved sample with a two-phase lead-rich PbSe ingot in an evacuated quartz ampoule at 560°C for one hour.¹² A junction depth of 40 μ below a cleaved (100) surface was obtained. A Fabry-Perot cavity was formed by cleaving two reflecting planes perpendicular to the junction. Typical laser dimensions are $0.40 \times 0.18 \times 0.18 \text{ mm}$, the longer dimension being the distance between the reflecting faces. Unannealed PbSe has shown no laser action and substantially less injection luminescence than the annealed material.

The diodes were mounted on a conduction-cooled block of a liquid helium dewar with BaF_2 windows. Forward current was supplied in 4- μ sec pulses. Figure I-4 shows the spectra above and below the threshold for stimulated emission for a diode at approximately 12°K. The spectra have been normalized to illustrate line narrowing. The average wavelength separation between modes is 227 Å. Using the usual expression for the mode spacing in a Fabry-Perot cavity, a room-temperature value of 4.8 for the refractive index,¹³ and neglecting the dispersion term, the mode separation is calculated to be 187 Å. This value is in good agreement with the experimental result. The 65-Å width of the main peak in Fig. I-4 is resolution limited.

Figure I-5 is a plot of radiation intensity from the cleaved end of the diode as a function of forward diode current. The steep rise at 3.9 amp indicates the onset of laser action at a threshold current density of 5600 amp/cm². Results of observations of the radiation spectrum as a function of current confirm this threshold value.

Laser action in PbSe suggests that this material possesses a direct-gap band structure, in agreement with results of Shubnikov-deHaas effect studies.¹⁴ It is of interest that laser action in PbSe occurs at a wavelength well within the 8- to 14- μ "atmospheric window."

J. F. Butler	A. J. Strauss
A. R. Calawa	R. H. Rediker
R. J. Phelan, Jr.	

C. ELECTRON-BEAM-PUMPED GaAs LASER

Recently, line narrowing in CdS (Ref. 15) and laser action in InSb and InAs (Ref. 16) have been reported when electron-hole pairs were generated by means of a beam of high-energy electrons. An earlier attempt by others¹⁷ to obtain population inversion in GaAs and germanium was unsuccessful. We wish to report the observation of laser action in GaAs at liquid helium temperature when excited by a beam of 50-keV electrons.

The laser sample was prepared from p-type GaAs with a net acceptor density of $9.3 \times 10^{18} \text{ cm}^{-3}$ by cleaving a face perpendicular to the two parallel polished faces of a 0.21-mm-thick slice of the material. It was then soldered with tin on the cold finger of a liquid helium cryostat. High-energy electrons were supplied by an electron gun of the type used in a 7NP4 television projection kinescope which was mounted in such a way as to share a common vacuum with the cryostat. The electron beam was focused on the cleaved end of the sample, and the light was emitted perpendicular to the polished faces which formed the optical cavity. The beam current was supplied in 0.2- μ sec pulses at a repetition rate of 1000/sec, and the diameter of the focused beam was approximately 0.5 mm. An artist's representation of the electron-gun cryostat system is shown in Fig. I-6. The mounting of the laser sample is shown in detail in Fig. I-7.

Section I

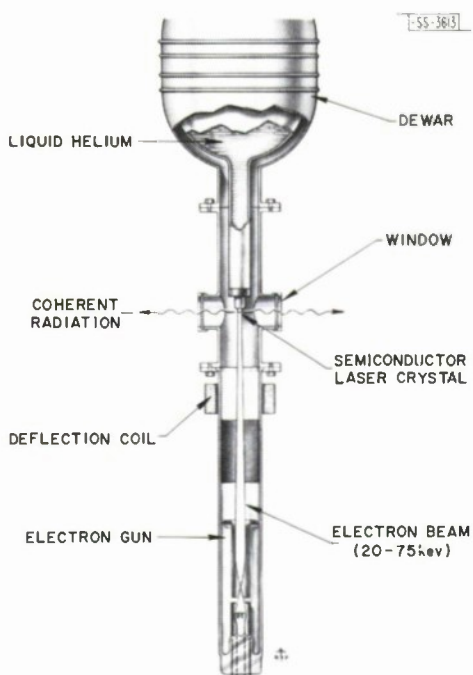


Fig. I-6. Artist's representation of electron-gun cryostat system.

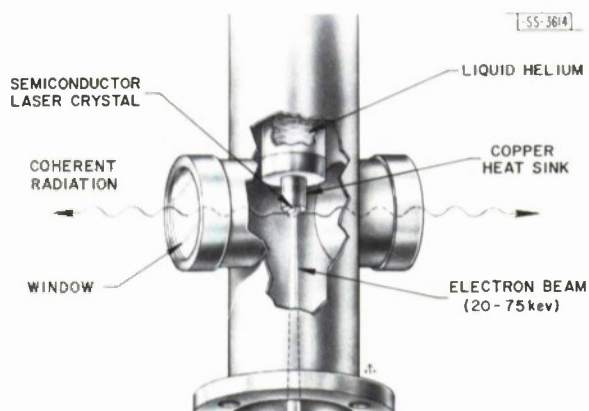
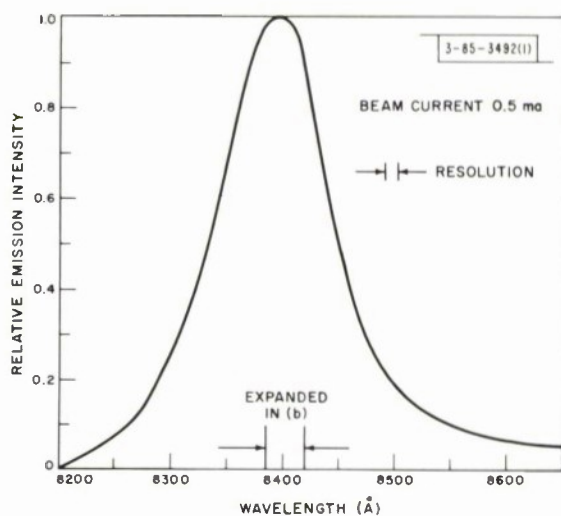
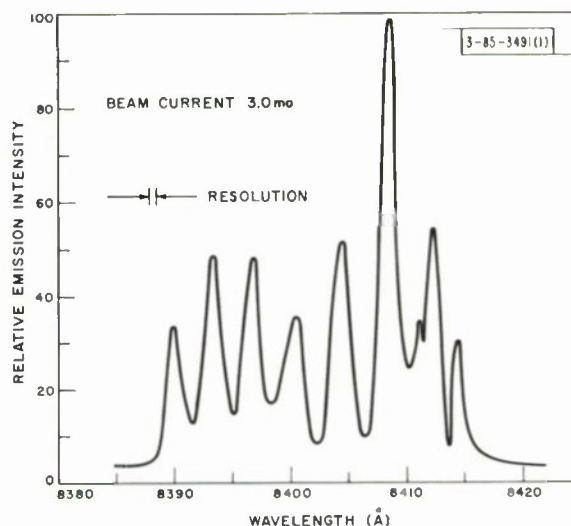


Fig. I-7. Artist's representation showing in detail the mounting of loser sample in electron-gun cryostat system.



(a)



(b)

Fig. I-8. Spectro of infrared emission from electron-beam-pumped GoAs at liquid helium temperature, below (0.5-ma beam current) and above (3.0-ma beam current) loser threshold. Width of expanded wavelength scale used in (b) to show mode structure of loser diode is indicated for comparison in (a).

Since for 50-kev electrons, the rms penetration depth¹⁸ is approximately 5μ and the extrapolated penetration depth¹⁹ is about 10μ , the thickness of the active region will be somewhere between these two values. The electron energy is also sufficiently low so as not to introduce radiation defects into the lattice.²⁰

Emission spectra of the sample below and above threshold are shown in Fig. I-8. Both the spontaneous line and the mode structure of the laser line are similar to those reported for GaAs laser diodes under pulsed operation.²¹⁻²³ The average wavelength separation between the modes is 3.5 \AA . Using the usual expression for mode spacing in a Fabry-Perot cavity and the value of 5.4 for $(n - \lambda dn/d\lambda)$ obtained²⁴ for lightly doped material at 2°K , the calculated mode spacing is 3.1 \AA for the cavity length of 0.21 mm. As has been observed in GaAs pulsed lasers,²⁵ the laser emission moved to longer wavelengths with time during a given pulse, which was presumably due to a shifting from one cavity mode to another caused by heating. This heating effect causes the excited cavity mode spacing to be somewhat greater than the 3.1 \AA predicted by the simple isothermal theory.²⁶

The intensity of the emitted radiation varied approximately linearly with the beam current at low current. Above 2 ma, the intensity rose rapidly indicating the onset of laser action. This corresponds to a threshold beam current density of about 1 amp/cm^2 . Assuming that the mean total energy¹⁸ required to produce a pair in GaAs is 5 ev and neglecting any backscattering of the 50-kev electron beam, this is equivalent to a threshold current density of 10^4 amp/cm^2 in a diode laser. Backscattering of the beam may reduce this value by as much as 50 percent.²⁷

The sample emission was also viewed through a "snooperscope" and, as observed in GaAs diode lasers, the emission was very intense at spots along the edge of the crystal, indicating that laser action was probably taking place in narrow filaments along the cleaved surface. Since the beam spot size was smaller than the width of the sample (1 mm) in the direction perpendicular to the cavity, the beam could be swept along the cleaved surface, thereby preferentially exciting one or more filaments.

The technique of electron-beam pumping will hopefully permit laser action to be obtained in those semiconductors in which it is difficult to produce good p-n junctions or in which resistivities are so high that series resistance and consequent heating preclude the use of electrical injection.

C. E. Hurwitz	R. H. Rediker
R. J. Keyes	P. Youtz
A. R. Calawa	B. Lax

D. ROOM-TEMPERATURE GaAs PULSED-LASER TRANSMITTER

It has been shown that 4 watts of peak power at 0.91μ can be obtained from a GaAs laser at room temperature during a short pulse (several nanoseconds).²⁸ The scheme to be described uses a pnpn switching transistor, a capacitor, and a GaAs diode laser. Figure I-9 shows the circuit used.

While the pnpn switch is in the "off" mode, the capacitor C charges up to the applied voltage E_b by current through the resistor R and the diode laser. (This constitutes a reverse current which may damage the laser unless R is made sufficiently large.) A trigger pulse is then applied to "turn on" the pnpn switch so that the capacitor discharges quickly through the diode laser. Thus, it should be possible to make a complete room-temperature solid-state

Section I

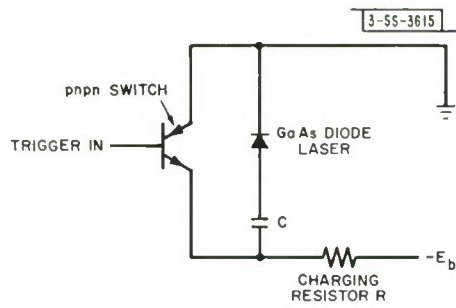


Fig. I-9. Schematic of solid-state diode laser pulse circuit.

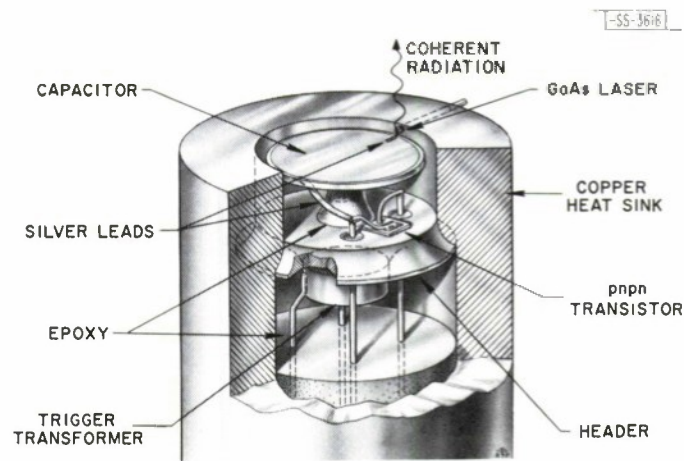


Fig. I-10. Artist's representation of miniaturized solid-state pulsed-laser-diode transmitter (excluding power supply and trigger).

Fig. I-11. Photograph of miniaturized pulsed-laser-diode transmitter.



P142-91

pulsed-laser-diode transmitter in a TO-5 transistor header. As a feasibility test, one such miniature transmitter has been mounted inside a small copper cylinder $\frac{1}{2}$ inch in diameter and about 1 inch long. Figure I-10 shows an artist's representation of this transmitter which has successfully operated at room temperature with $1\frac{1}{2}$ watts of peak power with a pulse length of 20 nsec. In Fig. I-11, the transmitter is compared in size with a penny. This room-temperature pulsed-laser system should have many applications in radar and other range-finding equipment.

T. M. Quist
G. F. Dalrymple (Group 42)

E. SCANNING INFRARED MICROSCOPE

In order to observe the pattern of infrared radiation from the surface of an InSb diode laser, a sensitive image converter was constructed. This converter, which uses a slow mechanical scanning system in conjunction with a synchronous detector, is able to display, on an oscilloscope, images of sources emitting radiation of wavelengths from the visible to 5.4μ . A magnification of about 25 times with a resolution of about 40μ was achieved.

The components of the system for looking at an InSb laser are shown in Fig. I-12. The phase-sensitive amplifier generates a signal which triggers the pulse generator. Current pulses from this generator yield pulses of infrared radiation from the InSb diode laser. This radiation is focused by an infrared lens, after reflecting off two front surface mirrors, onto an infrared detector. The two mirrors are mounted so that they rotate on two mutually perpendicular axes. As these mirrors rock back and forth, they scan the image from the diode laser across the detector. Potentiometers mechanically linked to the mirror positions yield voltages to drive the

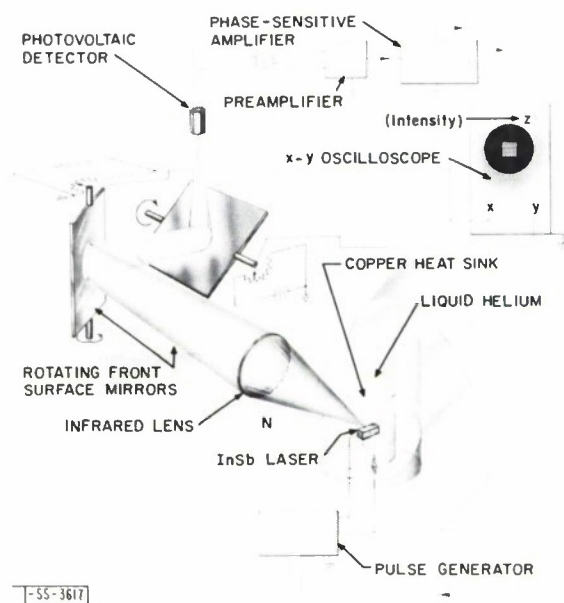


Fig. I-12. Infrared microscope system for displaying pattern of radiation at surface of electroluminescent diode.

Section I

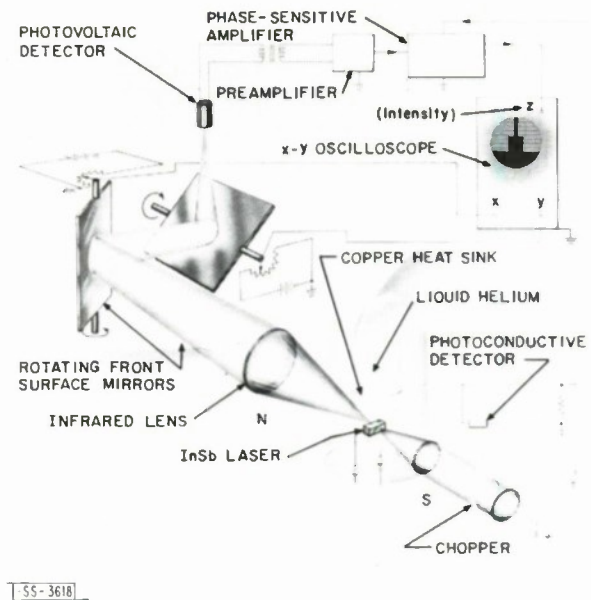


Fig. I-13. Infrared microscope system for obtaining shadow images.

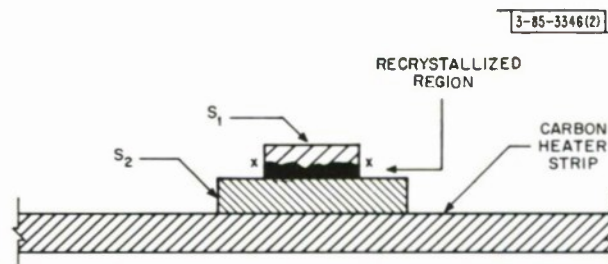


Fig. I-14. Experimental arrangement for interface alloying illustrating boundary x-x between nonmelted and recrystallized regions of semiconductor S₁ which has lower melting point than S₂.

x- and y-axes of an oscilloscope, and the output signal from the phase-sensitive amplifier is used to modulate the intensity of the oscilloscope trace. The complete picture is recorded on film by a time exposure of the trace. The laser was operated in the tail of a helium dewar between magnet pole faces as illustrated in Fig. I-12.

In order to determine the spatial location of the radiating regions, shadow images of the diodes were also displayed on the oscilloscope by the system illustrated in Fig. I-13. The light producing the shadow was chopped at about 1 kcps, and a phase signal for the amplifier was produced with a photoconductive detector. Both systems could be operated simultaneously by properly adjusting the intensity of the light source producing the shadow, and by using the photoconductor signal to trigger the pulse generator and provide the locking signal for the phase-sensitive amplifier.

The wavelength region for which this system may be utilized is limited only by the detector used and the transmission of the infrared lens and dewar windows. The detector was an InSb photovoltaic detector with close to optimum detectivity.

R. J. Phelan, Jr.
I. Melngailis

F. INVERSION OF $\{111\}$ SURFACES IN SINGLE-CRYSTAL REGROWTH DURING INTERFACE ALLOYING OF INTERMETALLIC COMPOUNDS

The technique of interface alloying has been used to produce single-crystal junctions between dissimilar semiconductors.²⁹ Oriented wafers are placed on a carbon heater strip (Fig. I-14) so that semiconductor S_1 , which has the lower melting point, is supported by semiconductor S_2 . Electrical current passed through the heater strip produces a temperature gradient such that S_2 is at a higher temperature than S_1 . As the temperature is raised, the lower face of S_1 begins to melt. However, before the entire wafer can melt, the heater strip current is turned off and, as illustrated in Fig. I-14, the melted portion recrystallizes having alloyed into S_2 .

Junctions have been fabricated by the above procedure between several pairs of the III-V compound semiconductors, and for $\{100\}$ -, $\{110\}$ -, and $\{111\}$ -oriented wafers. Junctions formed by mating $\{111\}$ faces pose a particular problem due to the polar nature of these zinc-blende semiconductors.³⁰ We have found that junctions produced by mating an A $\{111\}$ surface with a B $\{111\}$ surface have reproducible electrical characteristics. However, junctions formed by mating A $\{111\}$ to A $\{111\}$ and B $\{111\}$ to B $\{111\}$ surfaces exhibit mechanical weakness at the boundary x-x (Fig. I-14) between the nonmelted and recrystallized regions of S_1 . In this case, nonreproducible electrical characteristics are obtained unless the nonmelted region of S_1 is removed and an ohmic contact alloyed directly to the recrystallized region.

The mechanical weakness at x-x and the poor electrical characteristics are caused by an inversion of the diatomic layers which has taken place in the recrystallized region of S_1 . When the molten S_1 surface recrystallizes on the S_2 surface, it follows the orientation of this higher-melting seed. Thus for two wafers which originally had their A $\{111\}$ faces in contact, the recrystallized region is inverted with respect to the unmelted portion of S_1 , and an A $\{111\}$ -A $\{111\}$ boundary is created at x-x. A similar reorientation occurs for wafers which are initially B $\{111\}$ mated.

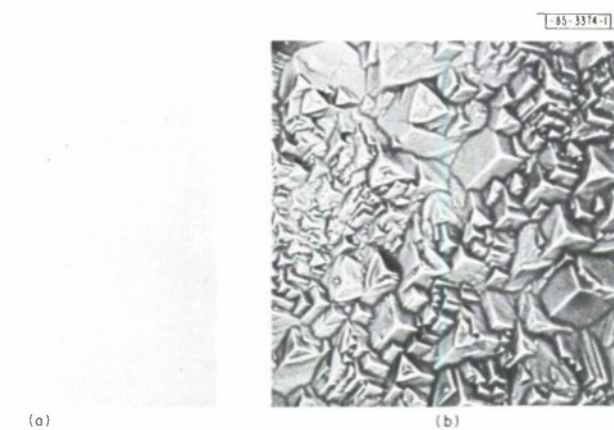


Fig. I-15. Etched upper surface of GoSb. A {111} face of GoSb was in contact with A {111} face of InAs before interface alloying. (a) Original unmelted B {111} surface. (b) A {111} surface of recrystallized region exposed by grinding off unmelted GaSb. (250X).

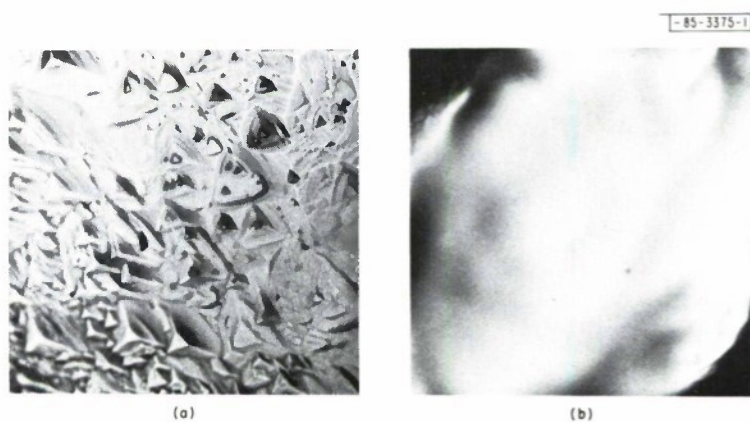


Fig. I-16. Etched upper surface of GoSb. B {111} face of GaSb was in contact with B {111} face of InAs before interface alloying. (a) Original unmelted A {111} surface. (b) B {111} surface of recrystallized region exposed by grinding off unmelted GaSb. (250X).

The diatomic inversion in the recrystallized region is evident from etching studies of semiconductor S_1 . It is well known that $A\{111\}$ surfaces develop etch pits in oxidizing etchants, whereas $B\{111\}$ surfaces do not.³⁰ An interface-alloy junction was made between 0.25-mm-thick wafers of GaSb (S_1 in Fig. I-14) and InAs (S_2 in Fig. I-14) where the $A\{111\}$ faces were mated. Figure I-15(a) shows the original $B\{111\}$ upper surface of the GaSb after a 15-sec etch in a solution of 10 percent bromine in methyl alcohol. (The same etchant was used in all cases.) The GaSb was ground down approximately 0.15 mm to expose the recrystallized region, polished, and etched. The upper surface of this region shows definite oriented etch pits [Fig. I-15(b)] characteristic of an $A\{111\}$ face, indicating that the recrystallized region had inverted and had grown as a single crystal emanating from the InAs interface.

A similar set of photomicrographs is presented (Fig. I-16) for an interface-alloy junction between two $B\{111\}$ faces of GaSb and InAs. Figure I-16(a) illustrates the original etched $A\{111\}$ upper surface of the GaSb. Figure I-16(b) illustrates the etched recrystallized $B\{111\}$ surface of the GaSb approximately 0.20 mm below the original surface. It is apparent that atomic layer inversion has taken place for these B:B mated wafers, as it did for the A:A case.

E. D. Hinkley
R. H. Rediker
Mary C. Lavine

G. CW GUNN EFFECT OSCILLATOR

The Gunn effect oscillator³¹ has been operated with a DC applied voltage. All such oscillators have previously required pulsed voltages of about 1- μ sec duration in order to prevent overheating and burnout of the devices. Figure I-17 shows an artist's representation of the Gunn effect oscillator which has been operated CW at room temperature. The piece of n-type 25- μ thick, 125- μ square, 1-ohm-cm GaAs was alloyed with tin in a forming gas atmosphere between two disks of tin-clad molybdenum. This assembly was then alloyed to the copper stud, and epoxy was applied to provide stability and rigidity. The device was then mounted in a tunable coaxial cavity and a DC voltage of 9 volts was applied. Oscillations were observed with a spectrum analyzer at many frequencies, but predominantly at 5 Gcps. The 5-Gcps frequency is predicted from the equation originally presented by Gunn: $f = v_d/L$, where f is the frequency in cps, v_d the drift velocity of the electrons, and L the thickness of the GaAs. It is now necessary to terminate the oscillator with the proper impedance network so that single-frequency operation can be obtained.

T. M. Quist

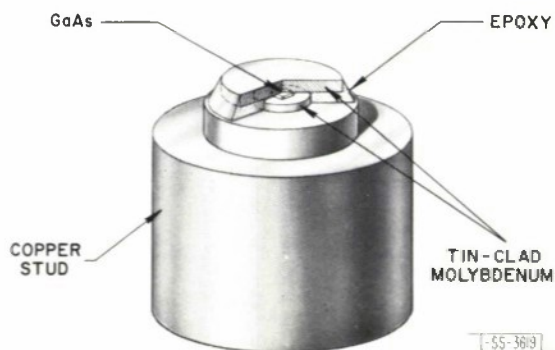


Fig. I-17. Artist's representation of CW room-temperature Gunn effect oscillator.

H. GROWTH OF $(\text{In}_x\text{Ga}_{1-x})\text{As}$ SINGLE CRYSTALS BY VAPOR PHASE REACTION

We have grown, by vapor phase reaction, single crystals of $(\text{In}_x\text{Ga}_{1-x})\text{As}$ from which diodes have been fabricated that lased at 8720Å . This wavelength is within the $8750 \pm 50\text{-Å}$ range required to pump a Nd^{+3} laser efficiently. Contrary to early results in the mixed crystals, the laser action was readily achieved. Threshold current densities are now typically $\sim 3000\text{ amp/cm}^2$ at 77°K and in some cases are less than 2000 amp/cm^2 . In addition, the power output of these mixed-crystal diodes is essentially the same as that from good GaAs lasers. Two typical examples at 77°K are 1.5 watts at 10 amp and 1.2 watts at 7.5 amp. In both cases, the currents are ~ 2 times threshold.

The improvement in crystal quality that has enhanced the laser action is due in part to careful doping control ($\sim 10^{18}$ carriers/ cm^3 produced by introducing tellurium into the closed system). In addition, the mechanical properties of the crystals have been markedly improved by careful annealing after growth. This is indicated by the ease of cleaving, the excellent faces resulting from cleaving, and the low loss of material during cleaving.

The value of "x" for the indium in the mixed crystal used to produce lasers which radiate at 8720Å is ≈ 0.028 , as determined from lattice constant measurements.[†] This mol-fraction of 0.028 is lower than that actually introduced into the closed system. Preliminary data indicate, in fact, that for Cl_2 carrier gas there is a segregation of the indium during growth, and a few runs with AsI_3 as carrier indicate a different degree of segregation.

S. Stopek

[†] The measurements were performed by Mary C. Finn.

REFERENCES

1. G. E. Fenner and J. D. Kingsley, J. Appl. Phys. 34, 3204 (1963).
2. I. Melngailis, Bull. Am. Phys. Soc. 9, 269 (1964).
3. I. Melngailis and R. H. Rediker, Proc. IRE 50, 2428 (1962).
4. N. Holonyak, Proc. IRE 50, 2421 (1962).
5. R. S. Levitt, et al., IEEE Trans. on Electron Devices ED-10, 333 (1963).
6. R. J. Phelan, A. R. Calawa, R. H. Rediker, R. J. Keyes and B. Lax, Appl. Phys. Letters 3, 143 (1963).
7. R. L. Bell and K. T. Rogers, Appl. Phys. Letters 5, 9 (1964).
8. G. Burns and M. I. Nathan, Proc. IEEE 52, 770 (1964).
9. J. F. Butler, A. R. Calawa, R. J. Phelan, Jr., T. C. Harman, A. J. Strauss and R. H. Rediker, Appl. Phys. Letters 5, 75 (1964).
10. The first report of laser action in PbSe diodes was added, in galley proof, to Ref. 9.
11. K. Igaki and N. Ohashi, J. Phys. Soc. Japan 18 (Suppl. 2), 143 (1963).
12. J. F. Butler, J. Electrochem. Soc. 111, 1150 (1964).
13. A. K. Walton and T. S. Moss, Proc. Phys. Soc. 81, 509 (1963).
14. M. R. Ellett and K. F. Cuff, Bull. Am. Phys. Soc. 8, 601 (1963).
15. N. G. Basov, O. V. Bogdankevich and A. G. Devyatkov, Symposium on Radiative Recombination in Semiconductors, Paris, 28 July 1964.
16. C. Benoit á la Guillaume and T. M. DeBever, Symposium on Radiative Recombination in Semiconductors, Paris, 28 July 1964.
17. N. G. Basov and O. V. Bogdankevich, Zhur. Eksp. i. Teoret. Fiz. 44, 1115 (1963) [translation: Soviet Phys. - JETP 17, 751 (1963)].
18. M. Balkanski and F. Gans, Proceedings of the Conference on Luminescence of Organic and Inorganic Materials, New York, 1962, H. P. Kallman and Grace M. Spruch, eds. (New York University and Wiley, New York, 1962), pp. 318-333.
19. R. D. Evans, The Atomic Nucleus (McGraw-Hill, New York, 1955), p. 624.
20. R. Bauerlein, Z. Physik 176, 498 (1963).
21. R. N. Hall, G. E. Fenner, J. D. Kingsley, T. J. Soltys and R. O. Carlson, Phys. Rev. Letters 9, 366 (1962).
22. M. I. Nathan, W. P. Dumke, G. Burns, F. H. Dill, Jr., and G. Lasher, Appl. Phys. Letters 1, 62 (1962).
23. T. M. Quist, R. H. Rediker, R. J. Keyes, W. E. Krag, B. Lax, A. L. McWhorter and H. J. Zeiger, Appl. Phys. Letters 1, 91 (1962).
24. M. I. Nathan, A. B. Fowler and G. Burns, Phys. Rev. Letters 11, 152 (1963).
25. W. E. Howard, F. F. Fang, F. H. Dill and M. I. Nathan, Bull. Am. Phys. Soc. 8, 88 (1963).
26. W. E. Engeler and M. Garfinkel, J. Appl. Phys. 34, 2746 (1963).
27. G. F. J. Garlick, Proc. IRE 43, 1908 (1955).
28. C. C. Gallagher, P. C. Tandy, B. S. Goldstein and J. D. Welch, Proc. IEEE 52, 717 (1964).
29. R. H. Rediker, S. Stopek and J. H. R. Ward, Solid State Electronics 7, 621 (1964).
30. H. C. Gatos and M. C. Lavine, J. Electrochem. Soc. 107, 427 (1960).
31. J. B. Gunn, IBM J. Research Develop. 8, 141 (1964).

II. LASER RESEARCH

A. RAMAN LASER PROGRAM

1. Stimulated Raman Emission at 90° to the Ruby-Laser Beam

Work has continued on stimulated Raman emission at 90° to the ruby-laser beam beyond that reported in the last Solid State Research Report[†] and in Applied Physics Letters.¹

Output from a nitrobenzene-filled cavity with mirrors that reflect over 99 percent from 6940 to 9000 Å has been observed on a Jarrell-Ash photographic grating spectrometer at S_1 , S_2 , S_3 , and approximately 6943 Å. All the outputs have the spatial characteristics of a laser beam. The output at 6943 Å can be seen by the eye as a narrow laser-type beam emerging at 90° from the cavity. In order to see if this radiation has a 90° Brillouin frequency shift (4.25 Gcps) from the forward laser pump, external etalon photographs will be taken which show the radiation and the primary pump beam together. The threshold for S_1 is 2 Mw, for S_2 and 6943 Å it is about 3 Mw, and for S_3 it is about 5 Mw. The power in S_1 is 10 kw, in S_2 and 6943 Å it is estimated by eye to be about 1 kw, and in S_3 it is barely detectable.

Output from CS_2 in the same setup has also been observed at S_1 , S_2 , S_3 , and 6943 Å. The threshold for S_1 is 0.5 Mw, for S_2 it is roughly 1 Mw, and for S_3 it is 5 Mw. The threshold for 6943 Å is not well correlated with the other outputs. Output at S_1 was also observed with a 5-Mw unfocused beam. This indicates that the S_1 threshold is 30 Mw/cm², if it is assumed that the ruby rod is lasing strongly over an area of 0.16 cm², and that the cylindrical lens concentrates the beam 10:1 in one dimension.

Jane H. Dennis
P. M. Eisenberger

2. Enhancement of Stimulated Raman Scattering by an Off-Axis Cavity

Effects have been observed of a stimulated Raman scattering cavity which is oblique to the ruby-laser cavity. Placing a liquid-filled cell between two parallel mirrors, with the perpendicular to the mirrors at a small angle with the axis of the ruby-laser cavity, has produced oscillation of the stimulated first Stokes component S_1 between the two mirrors. Such enhancement of the S_1 component has been obtained previously at 90° (Ref. 1) and at 2.4° (Ref. 2). In the present experiment, AS_1 Raman scattering is also observed, which peaks at the phase-matching angle with respect to the laser beam, as is usual, but whose peak value now depends on the orientation of the auxiliary cavity. The angular peak of the AS_1 goes through a maximum when the enhancement angle is the phase-matching angle for S_1 , and falls to zero at zero cavity angle, but falls only slightly for cavity angles up to several degrees above the phase-matching angle. Covering one or both of the mirrors drastically reduces the AS_1 (or S_1) signal.

D. L. Weinberg
F. H. Perry

[†] 1964:2, DDC 606126.

TABLE II-1
STIMULATED RAMAN EMISSION SPECTRA

Material	Raman Shift (cm^{-1})	Stokes Lines	Anti-Stokes Lines
Ethanol (1)	2921	1	—
Dimethylformamide (2)	2930	1	1
Methanol (1)	2831	1	—
Nitrobenzene (5)	1345	3	2
Calcite (5)	1084	3	2
Toluene (4)	1004	3	1
Carbon Disulfide (4)	656	3	1
Acetone (2)	2922	1	1
Chloroform (4)	667	3	1
Benzene (5)	992	3	1
	3062	1	—
Polystyrene (6)	1001	3	2
	3054	1	—
Trichlorethylene (3)	640	3	—
Trans-dichlorethylene (2)	2956	1	1
Cyclohexanone (7)	2863	1	1
	84	1	1
Dioxane (20)	836	4	3
	2856	1	1
	2967	1	1
Bromoform (148)	222	14	11
	539	6	4

3. Stimulated Raman Emission

In order to determine what parameters were of importance for the production of stimulated Raman emission, several materials were considered for their appropriateness in such an investigation. The materials and their observed spectra are noted in Table II-1. The number in parentheses after each material is the total number of lines that have been observed. This is larger than the number of Stokes and anti-Stokes lines (see Table II-1) when multiple scattering processes occur; the difference is the number of combination frequencies produced. Combination frequencies have also been seen for mixtures of liquids. The measurements were made with a giant-pulse-operated three-inch ruby laser and a Bausch and Lomb 1.5-m spectrograph.

S. Kern
B. Feldman

4. Experiments to Convert Stimulated Raman Excitation into Infrared Radiation

Experiments are planned to convert the optical phonons produced in stimulated Raman scattering into a coherent pulse of infrared radiation of the same frequency, as has been proposed.³⁻⁵ Any such production of infrared photons will be amplified by the phonon field only if the wave-number vector of the phonons is appropriate for photons of the same energy. This can be achieved by using a liquid with suitable dependence of refractive index on wavelength or by using crystal anisotropy. Such an arrangement would be an infrared source of high monochromatic peak power, with the possibility of operating even at very long infrared wavelengths.

D. L. Weinberg

B. GASEOUS DISCHARGE PRODUCED BY A GIANT-PULSED RUBY LASER

A study is being made of the decay properties of the discharge produced in several different gases by a giant-pulsed ruby laser. This study of the loss mechanisms in the discharge is fundamental to the determination of the breakdown mechanism itself. The time, pressure, and wavelength dependence of the afterglow radiation were measured for several noble and diatomic gases. From these measurements, conclusions can be drawn as to the probable dominant loss mechanism for each gas and a comparison can be made with the loss mechanism for discharges produced by more conventional techniques.⁶ Laser-produced discharges differ from conventionally produced discharges in several ways:

- (1) The laser pulse decays in about 10 nsec or less, so that the discharge can be studied for times shortly after the excitation.
- (2) The gas pressures are typically 1 atmos or greater compared to 1/10 atmos or less for the conventionally produced discharges.
- (3) The excitation mechanism is probably different,⁷ and thus the decay properties for short times following the excitation might possibly be different.
- (4) The plasma densities produced by the laser pulses are typically 10^{18} electrons/cm³, which is several orders of magnitude greater than those of conventionally produced plasmas.

The emphasis of the laser-produced discharges, to date, has been on the argon and hydrogen gases, with some work on helium, nitrogen, oxygen, carbon monoxide, and carbon dioxide. Only the preliminary results for argon and hydrogen are given in this report.

TABLE II-2 PARAMETERS FOR CALCULATING ELECTRON TEMPERATURE IN ARGON					
λ (Å)	E^\dagger (ev)	Transition [†]	J	f	g
7514.65	13.272	$2p_5 \rightarrow 1s_4$	1	0.093	3
7503.87	13.479	$2p_1 \rightarrow 1s_2$	1	0.12	3
†C. E. Moore, Atomic Energy Levels, NBS Circular 467 (1949).					

TABLE II-3 STARK PROFILE PARAMETERS FOR CALCULATING ELECTRON DENSITIES IN ARGON (T = 5000°K)			
λ (Å)	ω Full Halfwidth (measured)	ω'^\dagger Full Halfwidth (theoretical)	Electron Density ($\times 10^{18} \text{ cm}^{-3}$)
7724	24.5 Å	0.0511 Å	2.4
7503	24.5	0.0487	2.52
6965	21.1	0.0409	2.58
† Full halfwidth for $n_e = 10^{16} \text{ cm}^{-3}$; to convert to electron density n_e , multiply by $(\omega/\omega') 10^{16} \text{ cm}^{-3}$.			

1. Argon

The emission spectrum of the laser-produced discharge in argon at 1 atmos has been measured. The majority of the spectral lines have been identified as belonging to either the first or second spectra of argon, i.e., they are either neutral-argon or singly ionized-argon lines.

The electron temperature and electron density were calculated from the details of certain spectral lines. The electron temperature was measured from the relative intensities of two lines of Ar^I, 7514.65 and 7503.87 Å, using the relation⁸

$$kT = \frac{E_1 - E_2}{\ln \frac{I_2 \lambda_2^3 g_1 f_1}{I_1 \lambda_1^3 g_2 f_2}}$$

where

- E_i = excitation energy of state i
- I_i = total intensity per wavelength interval
- λ_i = wavelength
- g_i = statistical weight of lower line = $2J + 1$
- J = total angular momentum
- f_i = absorption oscillator strength.

This expression follows from the Boltzmann distribution relation. The values for these parameters are listed in Table II-2. The electron temperature is calculated to be $T = 5300^\circ\text{K}$ which is reasonable for gases at 1 atmos. The electron density was calculated from expressions given by Griem⁹ for Stark broadening of spectral lines in dense plasmas. The electron densities calculated from the Stark profiles of three spectral lines are given in Table II-3. The average electron density is $n_e = 2.5 \times 10^{18} \text{ cm}^{-3}$ and corresponds to about 10 percent of all argon atoms present. This large value of n_e is consistent with estimates made by Meyerand and Haught¹⁰ and by Pedersen and Schlier.¹¹ However, these values of electron temperature and density must only be taken as tentative because we assumed the plasma was optically thin, and the effect of self-absorption on the line profile was ignored. It is believed that taking these effects into account will alter the n_e and T values slightly.

The decay curves for three different ruby-laser-created discharges in argon are shown in Fig. II-1. Using a gated photomultiplier for increased sensitivity, the discharge afterglow has been measured to persist for at least 1 msec after the ruby pulse. The decay mechanism appears to change about 1 µsec following the ruby pulse. This portion of the afterglow has not yet been investigated in detail.

The dominant loss mechanism for argon according to the data, as outlined below, appears to be volume electron-ion recombination with negligible losses due to diffusion and attachment. The data do not fit a diffusion loss mechanism. For electron-ion recombination, the rate of loss of electrons is

$$\frac{\partial n_e}{\partial t} = -\alpha n_e n_+ \approx -\alpha n_e^2 \quad (1)$$

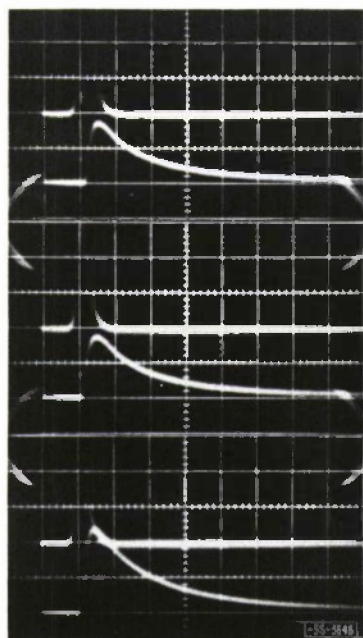


Fig. II-1. Time dependence of radiation from ruby-laser-produced spark in argon. Ruby giant pulse is shown in upper trace and radiation from spark is shown in lower trace. Spark radiation is limited to a spectral region from about 3000 to about 5750 Å by a CuSO_4 solution filter. Time scale is 100 nsec/cm for all traces; gas pressure is 1 atm.

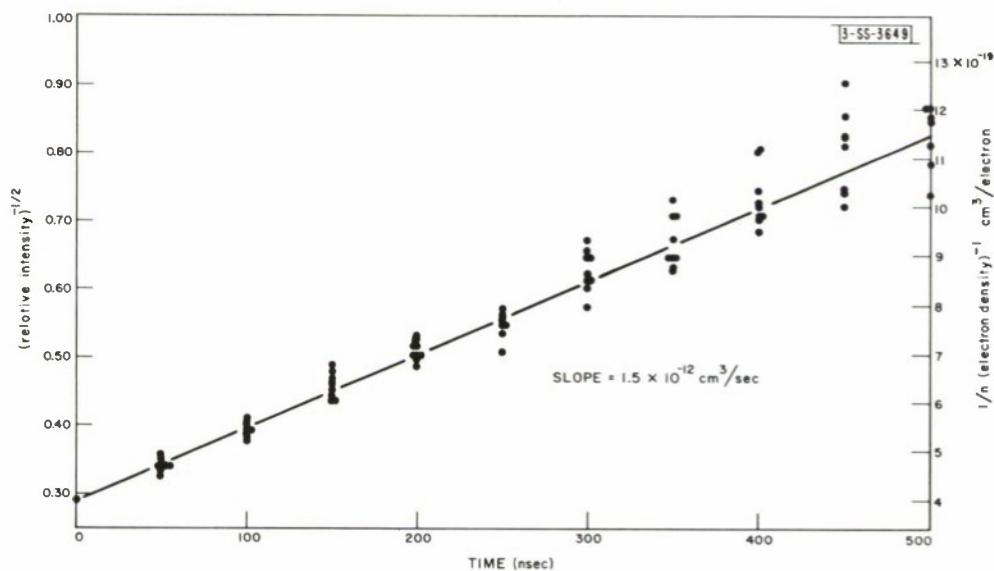


Fig. II-2. Electron-density decay as a function of time in argon at 1 atm.

where n_e and n_+ are the electron and ion densities, respectively, and α is the recombination coefficient. Because of electrical neutrality, $n_e \approx n_+$.

Solving for n_e , for α independent of n_e , one obtains

$$\frac{1}{n_e} = \frac{1}{n_e(0)} + \alpha t \quad (2)$$

The intensity of the radiation as measured by the phototube (Fig. II-1) is proportional to the square of the electron density.¹² This relation is based on the assumption that the recombination into an excited argon state is balanced by the radiative decay of that state.

Rewriting Eq. (2) in terms of light intensity, we find

$$I^{-1/2} = I_0^{-1/2} + \alpha ct \quad (3)$$

where c is the proportionality constant, $n_e = cI^{1/2}$. A plot of $I^{-1/2}$ vs t is shown in Fig. II-2 for the first 500 nsec following the ruby pulse. The data exhibit the recombination law dependence of Eqs. (2) and (3). The recombination coefficient α is calculated from the slope of Fig. II-2 to be

$$\alpha = 1.5 \times 10^{-12} \text{ cm}^3/\text{sec}$$

where c is evaluated from the electron density (Table II-3) at the peak of the intensity.

The pressure dependence of the $1/e$ decay time of the argon discharge is shown in Fig. II-3 for pressures from 1 to about 80 atmos. For lower pressures, the decay time decreases linearly with the logarithm of the pressure at a slow rate. For the high-pressure region, i.e., $p > 30$ atmos, this rate is about 2.7 nsec/atmos.

The dominant loss mechanism can be determined by a comparison of our results with those of Biondi.¹² He has studied the decay mechanism for microwave-produced discharges in argon at low pressures (about 10 mmHg) and small electron densities (about $3 \times 10^9 \text{ cm}^{-3}$); however, a qualitative comparison should be valid. Biondi finds that linear recombination of the type

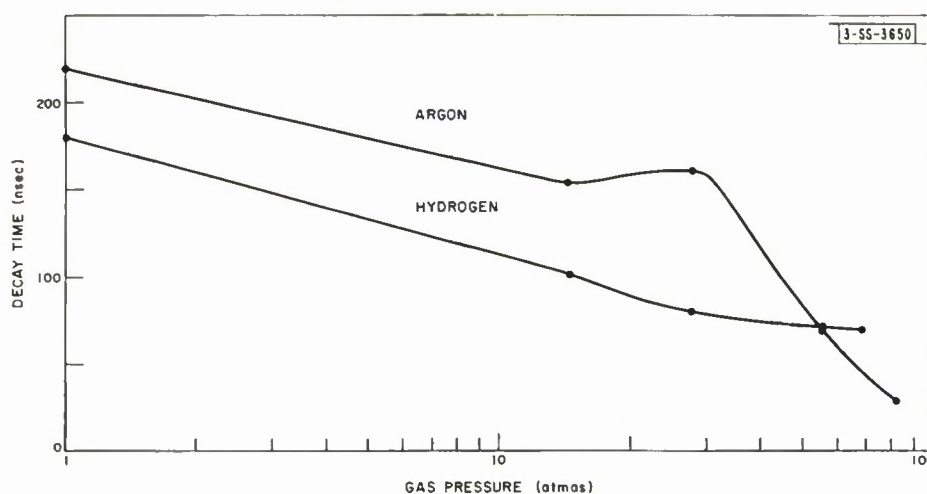


Fig. II-3. Pressure dependence of afterglow decay time in argon and hydrogen.

Section II

shown in Fig. II-2 requires the presence of molecular positive ions. The pressure dependence of the decay time (Fig. II-3) is opposite to that Biondi found for dissociative recombination. From this pressure dependence and the linear recombination of Fig. II-2, we can conclude that the mechanism is not that of dissociative recombination. The recombination coefficient calculated from Fig. II-2 ($\alpha \approx 1.5 \times 10^{-12} \text{ cm}^3/\text{sec}$) agrees approximately with the theoretical estimate of Stueckelberg and Morse¹³ ($\alpha \approx 10^{-12} \text{ cm}^3/\text{sec}$) but is smaller than that found by Biondi ($\alpha = 6 \times 10^{-7} \text{ cm}^3/\text{sec}$) and by Kenty¹⁴ ($\alpha = 2 \times 10^{-10} \text{ cm}^3/\text{sec}$). Part of this discrepancy might be attributed to the wide variation in electron densities (a ratio of $10^{10}:1$) and gas pressures (a ratio of 100:1) for the two experiments. Further investigations are necessary to clarify this point.

2. Hydrogen

The emission spectrum of the laser-produced discharge in hydrogen at 1 atm has been measured. The spectrograph consists of the Balmer series lines plus continuum. The electron density was estimated from the Stark profile of H_α to be $n_e \approx 10^{18} \text{ cm}^{-3}$. The continuum was too dense on the spectrogram for an accurate determination of the electron temperature. A simple modification of the experimental equipment should rectify this problem.

The decay curves for hydrogen are shown in Fig. II-4 and are similar to those for argon (Fig. II-1). Here, however, the decay is not a simple $1/n$ type of Eq. (2) over the entire time range but a composite of at least two decay curves. This is demonstrated to be the case by inserting band-pass filters between the discharge and the photodetector. When this is done, it is found that the "fast" decay comes from the spectral region $\lambda < 5400 \text{ \AA}$. Work is in progress to identify these two decay times further.

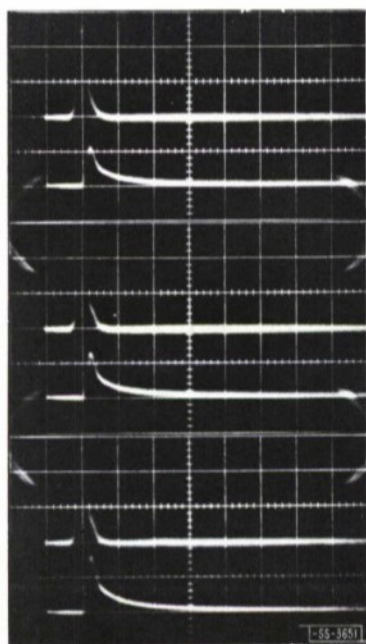


Fig. II-4. Time dependence of radiation from ruby-laser-produced spark in hydrogen at 1 atm. Time scale is 100 nsec/cm for all traces.

The pressure dependence of the $1/e$ decay time for hydrogen is shown in Fig. II-3. The decay time decreases approximately linearly with the logarithm of the pressure at a slow rate for the pressure range investigated.

The results are incomplete, but tentative conclusions indicate that the recombination mechanism for hydrogen is of the type given by Eq. (2). Diffusion effects are negligible. The recombination coefficient is estimated (order of magnitude) to be about $\alpha \approx 10^{-12}/\text{cm}^3$ (Ref. 15). Here again the discrepancy might be in the fact that we are dealing with high-density plasmas and high-pressure gases.

D. F. Edwards

C. PERTURBATION OF THE REFRACTIVE INDEX OF AN ABSORBING MEDIUM BY A LASER BEAM

Interferometer measurements have been made of the changes in refractive index associated with the heating of an absorbing medium by a laser beam. The order of magnitude of the change in refractive index which is observed can be estimated from the thermal expansion of the medium:

$$\Delta n = \frac{(n-1) (\text{volume expansivity})}{(\text{heat capacity}) (\text{density})} (\text{energy absorbed/unit volume})$$

where Δn , the change in the index n , ranges from 10^{-3} to 10^{-6} , depending upon whether a solid, liquid, or gas is used. To measure Δn , the apparatus shown in Fig. II-5 has been built. It consists of a neodymium glass laser (1.06μ) whose beam is fired into the absorbing medium placed in one arm of a Mach-Zehnder interferometer. The source for the interferometer is a pulsed argon gas laser (4880 \AA). Provision is made for time-resolved measurements by first triggering the neodymium laser (1 to 5 joules output in a spike train of 0.5 to 1 msec) and then, at some adjustable later time, triggering the argon gas laser (1 to 2 watts output in a 50-nsec pulse) to photograph the interferometer fringes. Future modifications will include some type of rapid framing or streaking for the camera during a single neodymium-laser pulse.

The media are chosen so that they absorb enough of the $1.06\text{-}\mu$ radiation to perturb the index, but pass essentially all the $4880\text{-}\text{\AA}$ interferometer beam. Unlike solids and liquids, suitable gases with reasonable absorption lengths are difficult to find. Significant changes have been observed for several solid, liquid, and gas media.

Figure II-6(a-c) shows the disturbance in the interferometer fringes produced by the absorption of between 1 and 2 joules of the $1.06\text{-}\mu$ beam in a 22-cm cell of methyl alcohol. The times indicated under the figures are the delays between the start of the neodymium glass laser and the photograph of the fringes. The absorption of energy in this case is so large that turbulence in the liquid obliterates the fringes. After 3 msec, the disturbance has grown to about twice the original beam diameter of the neodymium glass laser, and continues to grow for nearly a second when it is dissipated.

Figure II-7(a-e) shows similar photographs of a 1-m cell filled with monoethylamine gas which has a small absorption at 1.04μ . It is estimated that the cell absorbs about 1 percent of the 1 to 2 joules in the $1.06\text{-}\mu$ beam. These pictures are taken as before except that the interferometer is adjusted for infinite fringes (i.e., the two beams are rendered parallel and the

Section II

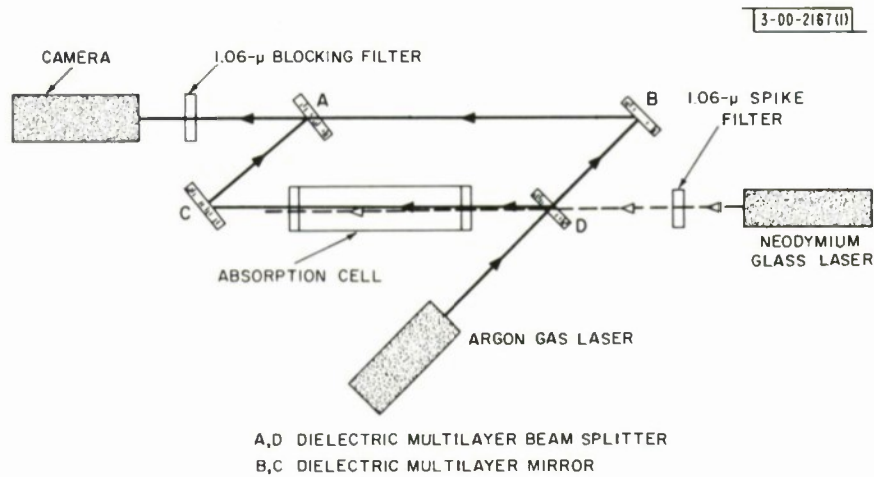
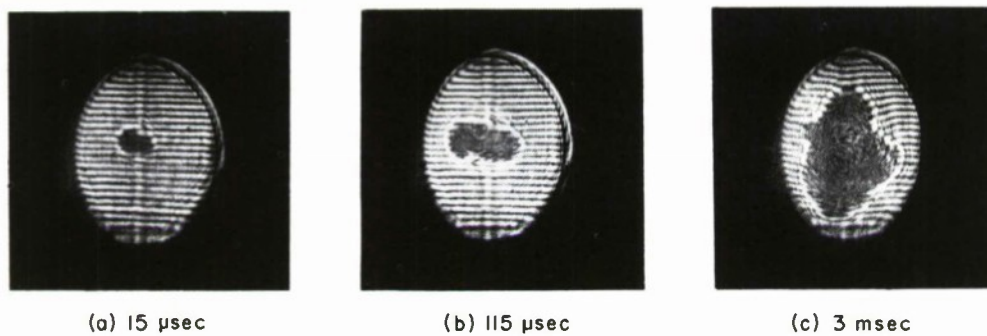


Fig. II-5. Schematic diagram of apparatus for measuring changes in refractive index of absorbing medio.

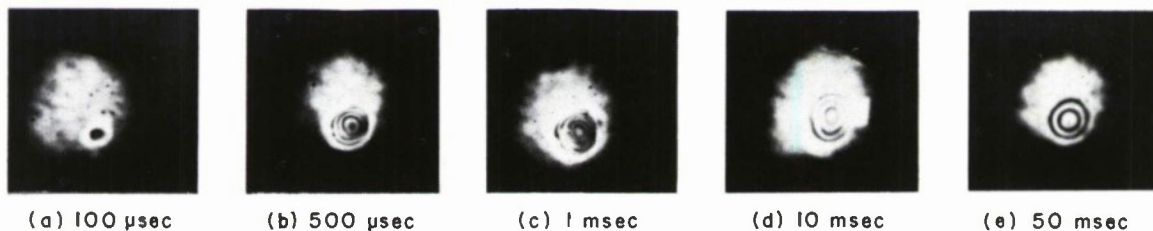


(a) 15 μsec

(b) 115 μsec

(c) 3 msec

Fig. II-6(a-c). Interferograms of disturbance of refractive index in 22-cm cell of methyl alcohol.



(a) 100 μsec

(b) 500 μsec

(c) 1 msec

(d) 10 msec

(e) 50 msec

Fig. II-7(a-e). Interferograms of disturbance of refractive index in 1-m cell of monoethylamine gas.

field is completely light or dark with a fringe spacing of infinity). When disturbed, the interferometer produces fringes of constant index of refraction. As expected, these fringes are fairly symmetric about the beam axis. The pattern, in this case, is equivalent to an average index profile which increases almost linearly from the center of the beam and which produces an interferometer beam divergence of about 1 mrad. Studies are under way to separate the effects of a non-uniform 1.06- μ beam intensity from those of the transport phenomena in the absorbing medium.

In addition to these relatively slow changes in index, rapid changes associated with sonic shock waves should be present. Effects of this nature have not yet been observed because the laser energy is being deposited too slowly, by several orders of magnitude, to produce strong shock waves. To remedy this, the experiments will be repeated using a Q-spoiled neodymium laser.

P. R. Longaker
J. D. Kuppenheimer, Jr.
M. M. Litvak

REFERENCES

1. J. H. Dennis and P. E. Tannenwald, Appl. Phys. Letters 5, 58 (1964).
2. H. Takuma and D. A. Jennings, Appl. Phys. Letters 4, 185 (1964).
3. H. J. Zeiger and P. E. Tannenwald, Proc. 3rd Internat. Conf. on Quantum Electronics 2, 1589 (1964).
4. E. Garmire, F. Pandarese and C. H. Townes, Phys. Rev. Letters 11, 160 (1963).
5. R. Y. Chiao, E. Garmire and C. H. Townes, Lecture at International School of Physics "Enrico Fermi," Varenna, Italy, August 1963.
6. H. G. Griem, Plasma Spectroscopy, Chap. 9 (McGraw-Hill, New York, 1964).
7. J. K. Wright, Proc. Phys. Soc. 84, 41 (1964); S. Rand, Phys. Rev. (to be published).
8. H. G. Griem, op. cit., p. 269.
9. Ibid., Chap. 4.
10. R. A. Meyerand and A. F. Haught, Phys. Rev. Letters 13, 7 (1964).
11. N. Pedersen and R. Schlier (private communication).
12. M. A. Biondi, Phys. Rev. 129, 1181 (1963).
13. E. C. G. Stueckelberg and P. M. Morse, Phys. Rev. 36, 16 (1930).
14. C. Kenty, Phys. Rev. 32, 624 (1928).
15. J. D. Craggs and W. Hopwood, Proc. Phys. Soc. 59, 771 (1947).

III. MATERIALS RESEARCH

A. ELECTRIC FURNACE FOR OPERATION IN OXIDIZING, NEUTRAL, AND REDUCING ATMOSPHERES TO 2400°C

Temperatures above 2000°C can be produced by resistance heating with tantalum, tungsten, molybdenum, or graphite heating elements in vacuum or neutral atmospheres. In oxidizing atmospheres, however, 1700°C is about the highest temperature which can be produced by direct resistance heating, using platinum or platinum alloy elements.¹ We have extended resistance heating in oxygen (or other atmospheres) to higher temperatures by developing a furnace in which a metal heating element that is operated in an inert atmosphere is used to heat a ceramic inner tube containing the sample in the desired atmosphere. This furnace, which employs a tantalum split-tube heating element protected by argon and an inner tube of dense zirconia, can be used to heat samples to 2400°C in an oxidizing atmosphere as well as in neutral or reducing atmospheres.

Figure III-1 is a schematic section view of the assembled furnace, which incorporates the base, power leads, and power supply of a commercial tantalum vacuum furnace (Centorr Associates) capable of supplying 8 kw at 600 amp. Water-cooled base (1) and lid (2) sections surround the whole furnace which is about 6 inches in diameter and 7 inches high. Two water-cooled current leads (3) supply current to the split tantalum heating element (4) which is 0.005 inch thick, 2 inches in diameter, and 3 inches high, with resistance of about 0.02 ohm at 2000°C. The element is surrounded on the top, bottom, and sides by tantalum heat shields (5). A dense zirconia tube (6), 1½ inches OD, 1⅜ inches ID, 6 inches long (Zirconium Corporation of America),

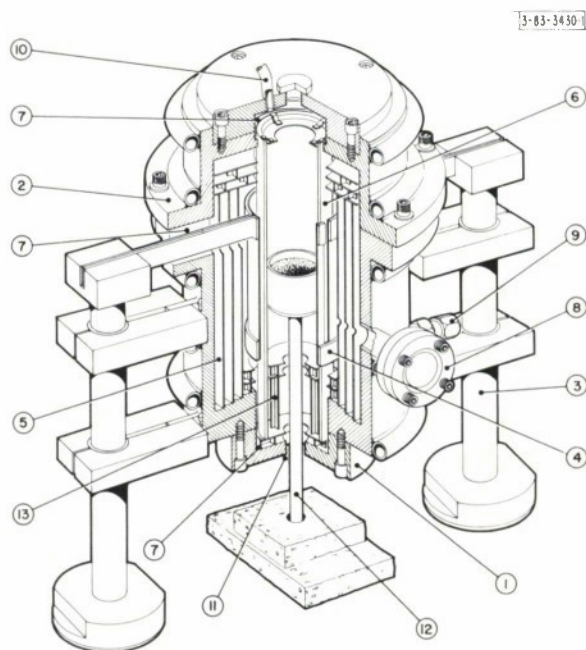


Fig. III-1. Schematic section view of assembled high-temperature furnace.

Section III

is mounted coaxially inside the heating element. The ends of the tube are loosely sealed to the base and lid sections with fibrous mullite (Fibrefrax) (7), which is also used for sealing around the current leads.

The heat shields contain holes lined up with a sight port (8) through which the temperatures of the heating element and zirconia tube can be measured pyrometrically. This port contains a gas inlet (9) for supplying argon to the heating element chamber. A gas inlet (10) for the zirconia tube and additional sight ports are included in the lid. There is a gas exit (11) in the base through which a refractory sample support rod (12) enters the hot zone. For some applications, it is desirable to place tantalum heat shields (13) inside the zirconia tube in order to reduce the thermal gradients in the hot zone and along the tube. The furnace has also been operated with a smaller heating element ($1\frac{1}{2}$ inches diameter) and a smaller zirconia tube (1 inch OD, $\frac{7}{8}$ inch ID, 6 inches long).

In a typical run, argon is first flushed through the heating element chamber at about 15 l/min. for 10 minutes, after which the rate is reduced to about 5 l/min. for operation. The desired gas is passed through the zirconia tube at about 5 l/min. The power is then raised gradually over a period of $\frac{1}{2}$ hour until the operating temperature is reached. After the run, the furnace is cooled to room temperature in about $\frac{1}{2}$ hour.

Typical data for the temperatures of the zirconia tube and a $\frac{1}{2}$ -inch-diameter magnesia sample pedestal are shown as a function of furnace power in Fig. III-2. These results were obtained in two runs, one with the 1-inch-OD zirconia tube and $1\frac{1}{2}$ -inch heating element, and the other with the $1\frac{1}{2}$ -inch-OD zirconia tube and 2-inch heating element. The temperatures were measured with a calibrated Pyro laboratory optical pyrometer. The pedestal was observed through a right-angle prism mounted on the furnace lid. The melting point of a sapphire sample observed through this prism was measured as 2050 °C, in good agreement with the published value.

Use of the zirconia tube in the furnace is advantageous even if the sample to be heated does not require an atmosphere harmful to the tantalum, since the zirconia protects the heating element

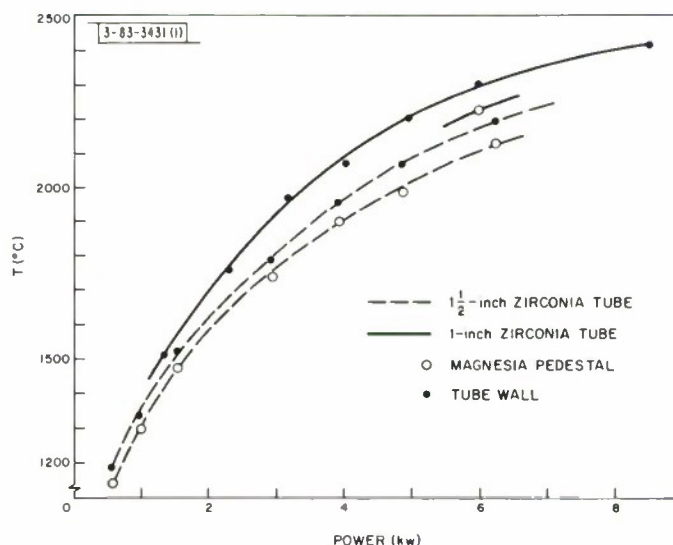


Fig. III-2. Measured temperatures of zirconia tube and sample pedestal as a function of furnace power.

from any volatile materials which may evaporate from the sample. In many cases in which tantalum furnaces are normally operated in vacuum, operation in argon may be more satisfactory. Argon decreases the rate of evaporation of both the tantalum heating element and the sample being heated, although it also reduces the rate at which volatile impurities are removed. Commercial argon has a nominal maximum impurity level of about 10 ppm (corresponding to an impurity partial pressure of 10^{-2} torr), but it is effectively gettered by the hot tantalum heat shields before it reaches the element or the sample.

It is expected that this furnace will find application in a variety of operations in the 1700° to 2400°C region, such as phase studies, material testing, diffusion study, and crystal growth. We have used it for the Czochralski growth of sapphire crystals with satisfactory results.

T. B. Reed
R. E. Fahey

B. ELECTRICAL PROPERTIES OF CrO_2

Measurements of the Seebeck coefficient α and resistivity ρ of polycrystalline CrO_2 samples prepared by high pressure synthesis² have been extended to liquid helium temperature. The stoichiometry of the samples used in these and previous experiments was measured by an analytical method³ which determines the chromium content with an accuracy of about 1 part per 1000.

Values of α and ρ measured between 12° and 440°K are plotted against absolute temperature T in Figs. III-3 and III-4, respectively, for samples with compositions of $\text{CrO}_{1.994}$ and $\text{CrO}_{2.015}$. For both samples, α is almost independent of T below 250°K, exhibiting neither the large increase due to phonon drag which is observed in single crystals of some materials at low temperatures, nor the decrease with decreasing temperature observed in the absence of phonon drag. It is suggested that phonon scattering at grain boundaries in these polycrystalline samples reduces the phonon drag effect to a level which is too small to produce an increase in α but sufficiently large to prevent a decrease in α as the temperature is decreased below 250°K. Above 250°K, the phonon drag effect is so small that α increases with increasing temperature, as observed in previous measurements on CrO_2 samples.^{4,5}

As shown in Fig. III-4, the resistivities of the $\text{CrO}_{1.994}$ and $\text{CrO}_{2.015}$ samples are about 5 milliohm-cm and change only slightly with temperature, although a small peak is observed in the vicinity of the Curie point (382°K) for the $\text{CrO}_{2.015}$ sample. These results are similar to those we obtained previously for samples of other compositions,^{4,5} but they differ markedly from those reported by Kubota and Hirota.⁶ The resistivities observed by these authors are about 2 orders of magnitude larger, decrease by factors of 2 to 3 when the temperature is increased from 200° to 600°K, and exhibit much larger peaks in the vicinity of the Curie point. We attribute these differences to the fact that our samples were prepared at much higher pressures than those of Kubota and Hirota.

The electrical properties of the samples studied in the present investigation, which have compositions ranging from $\text{CrO}_{1.89}$ to $\text{CrO}_{2.02}$, do not vary significantly over this composition range. This is consistent with the Goodenough model^{5,7} used to explain the metallic properties and ferromagnetism of CrO_2 , since according to this model such a change in stoichiometry would cause only a small relative change in the electron population of the (α) π^* -band responsible for conductivity.

J. M. Honig
J. A. Kafalas

Section III

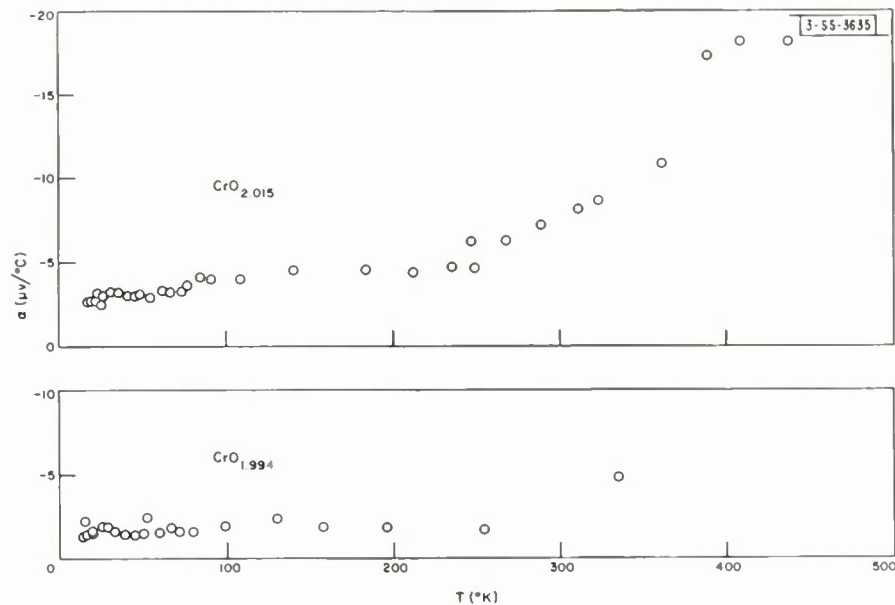


Fig. III-3. Seebeck coefficient α vs absolute temperature T for $\text{CrO}_{1.994}$ and $\text{CrO}_{2.015}$.

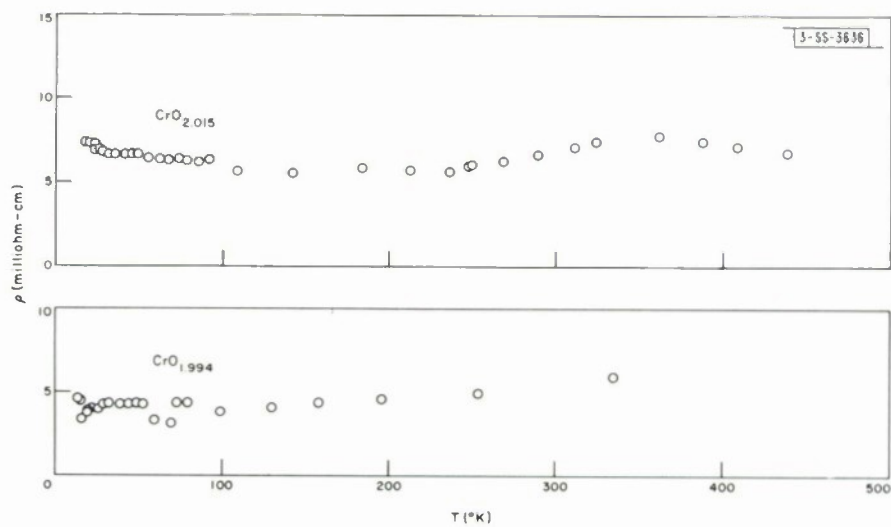


Fig. III-4. Resistivity ρ vs absolute temperature T for $\text{CrO}_{1.994}$ and $\text{CrO}_{2.015}$.

C. InSb-InTe SYSTEM

1. Phase Diagram

The phase diagram for the pseudo-binary InSb-InTe system, which has been determined by thermal, x-ray, and metallographic analysis, is shown in Fig. III-5. The complete diagram, which differs somewhat from a tentative version reported previously,⁸ includes not only the stable diagram (solid lines) but also portions of an unstable diagram (dashed lines). The data points shown give the temperatures of thermal arrests observed in cooling experiments.

In agreement with the earlier tentative diagram, Fig. III-5 shows that the ternary compound In_4SbTe_3 with rocksalt structure (first reported by Goryunova, Radautsan and Kiosse⁹) is a peritectic phase, unstable above 556°C. According to the stable diagram, InTe crystallizes as the primary phase when a melt containing more than 40 mol % InTe is cooled below its liquidus temperature. When this occurs, thermal arrests (indicated by closed circles in Fig. III-5) are observed at three temperatures: liquidus, peritectic, and eutectic. After the samples are cooled to room temperature, they are found by metallographic and x-ray examination to contain InTe, In_4SbTe_3 , and InSb. Figure III-6 is a photomicrograph which clearly shows all three phases in such a sample.

The stable diagram in Fig. III-5 also shows that In_4SbTe_3 is the primary phase which crystallizes from melts containing between 15 and 40 mol % InTe. For these samples, thermal arrests (open circles) are observed only at the liquidus and eutectic temperatures, and after solidification the samples contain only In_4SbTe_3 and InSb. Although inconsistent with the stable diagram, similar behavior has also been observed for many samples containing between 40 and 75 mol % InTe. This behavior reveals the existence of the unstable phase diagram shown in Fig. III-5, which was not included in the earlier tentative diagram. According to the unstable diagram, In_4SbTe_3 can crystallize as the primary phase from a melt containing more than 40 mol % InTe if the melt supercools far enough below the stable liquidus. Whether or not sufficient supercooling will occur depends on the experimental conditions. Reducing the cooling rate tends to increase the degree of supercooling.

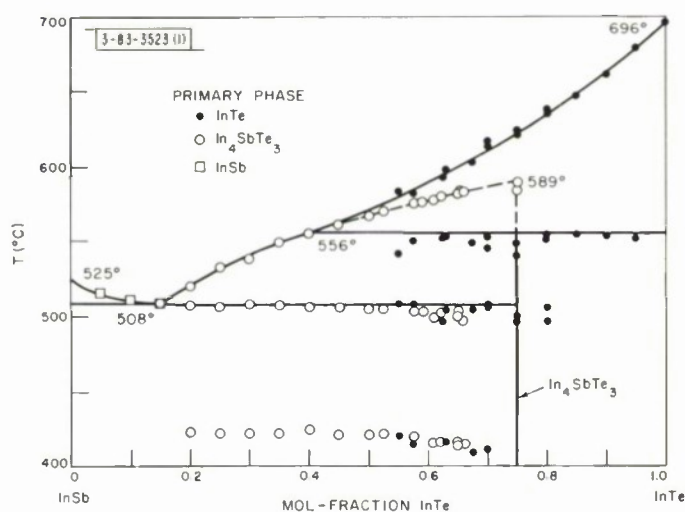


Fig. III-5. Phase diagram of pseudo-binary InSb-InTe system.

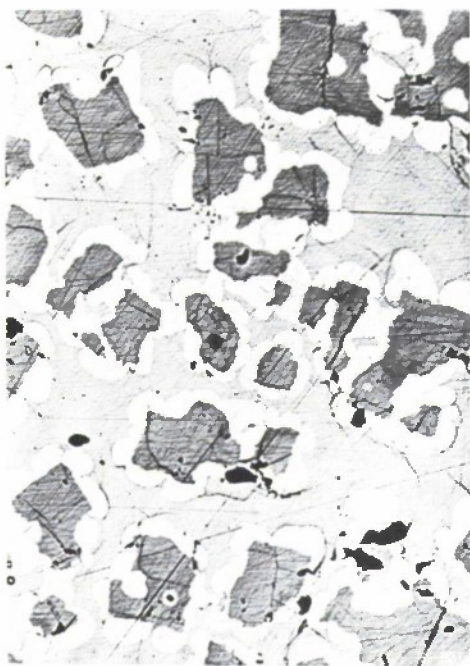


Fig. III-6. Photomicrograph of InSb-InTe sample prepared by solidification of melt containing 55 mol % InTe. Sample consists of dark islands of InTe (primary phase), each surrounded by a lighter ring of In₄SbTe₃, which is surrounded in turn by a darker matrix of InSb.

In their investigations of the InSb-InTe system, Goryunova, Radautsan and Kiosse,⁹ and Molodyan, Radautsan and Madan¹⁰ consistently obtained single-phase In₄SbTe₃ by slow cooling of melts containing 75 mol % InTe. (For this composition, Molodyan, *et al.*, observed a thermal arrest at 586°C, in good agreement with the unstable liquidus temperature of 589°C given in Fig. III-5.) Consequently, they failed to identify In₄SbTe₃ as a peritectic phase. When Molodyan, *et al.*, heated a sample of In₄SbTe₃, they observed a thermal arrest at 557° to 561°C, in good agreement with the peritectic temperature of 556°C given in Fig. III-5, which they attributed to decomposition of an unspecified character.

Liquidus temperatures for melts containing less than 15 mol % InTe are indicated by squares in Fig. III-5. Samples obtained by solidification of these melts consist of two phases, a solid solution of In₂Te₃ in InSb and a phase containing essentially pure indium which was identified by electron microprobe analysis. These phases do not lie in the InSb-InTe pseudo-binary section, but they are not stable, since they are no longer observed after the samples have been annealed for two to three weeks at 475°C. The phases present after annealing do lie in the pseudo-binary section. Samples containing up to about 5 mol % InTe are then single-phase solid solutions of InTe in InSb. Samples containing a higher percentage of InTe consist of two phases, InTe-saturated InSb and InSb-saturated In₄SbTe₃.

Small thermal arrests were observed at 410° to 430°C, as shown in Fig. III-5, in cooling runs on almost every sample containing between 20 and 70 mol % InTe. In the tentative phase diagram reported earlier, these arrests were attributed to a solid-state transformation in In₄SbTe₃. Further investigation has failed to confirm such a transformation. No thermal arrests below the eutectic temperature were observed in heating and cooling experiments on samples consisting almost entirely of In₄SbTe₃ (together with a small quantity of InSb), which were prepared by directional freezing of a melt containing 65 mol % InTe. Furthermore,

high-temperature x-ray diffraction measurements showed that up to 530°C there was no change in the crystal structure of In_4SbTe_3 and that the lattice constant increased linearly with temperature over the entire range. A monotectic arrest is observed at 423°C in thermal analysis experiments on samples of stoichiometric InTe. According to the phase diagram of Grochowski, *et al.*,¹¹ for the In-Te system, this arrest is observed because the composition at the congruent melting point of InTe is not stoichiometric. Consequently, an initially stoichiometric melt does not freeze congruently, and its stoichiometry changes with decreasing temperature. The low-temperature arrests observed in the present experiments might be similarly associated with the formation of a minor phase due to deviations from stoichiometry.

The compounds InSb, In_4SbTe_3 , and InTe are shown as line phases in Fig. III-5 because data on their homogeneity ranges are limited. The annealing experiments described above show that the solubility of InTe in InSb (zinc-blende structure) is about 5 mol % at 475°C. The lattice constant of InSb saturated with InTe is $6.470 \pm 0.002 \text{ \AA}$, compared with the value of $6.478 \pm 0.001 \text{ \AA}$ for pure InSb. X-ray diffraction data for InSb-InTe samples annealed at 475°C establish upper and lower limits of 80 and 70 mol % InTe, respectively, for the homogeneity range of In_4SbTe_3 , but the actual homogeneity range may be much smaller. The lattice constant for single-phase In_4SbTe_3 , prepared by annealing samples containing 75 mol % InTe, is $6.132 \pm 0.002 \text{ \AA}$. The lattice constant for In_4SbTe_3 saturated with InSb, which was obtained in measurements on a number of two-phase samples with average compositions between 10 and 65 mol % InTe, is $6.125 \pm 0.001 \text{ \AA}$. The solubility of InSb in InTe (TlSe structure) is less than 5 mol % at 475°C, according to x-ray diffraction data.

2. Superconductivity

It was reported previously⁸ that high-pressure samples of In_4SbTe_3 , prepared by melting at 37 kbar and quenching to room temperature before releasing the pressure, exhibited superconductivity at temperatures below about 1.5°K. Superconductivity was not observed down to 1.3°K, however, in a sample prepared at atmospheric pressure by directional freezing of a melt containing 40 mol % InTe. It was suggested that the difference in behavior resulted because the atmospheric pressure sample was saturated with InSb.

Further investigation has shown that similar differences in superconducting properties occur for high- and low-pressure samples even if they have the same composition. Thus single-phase In_4SbTe_3 samples prepared at low pressure by annealing mixtures containing 75 mol % InTe in evacuated ampoules failed to exhibit superconductivity down to 1.3°K, but after these samples had been annealed for an hour or more at 37 kbar and 475°C they exhibited superconducting transition temperatures of $1.5^\circ \pm 0.2^\circ \text{K}$, the same as observed for high-pressure samples of the same composition prepared from the melt. The samples were then annealed again under low pressure. After 30 hours at 400°C, the superconducting transition was reduced but still detectable, but after 8 to 26 hours at 475° to 500°C, superconductivity was not observed down to 1.3°K. X-ray diffraction measurements were made after the initial low-pressure, the high-pressure, and the final low-pressure anneals. These measurements showed that throughout the experiment each sample remained single phase, retained the rock-salt structure, and had the same lattice constant within the experimental error of 0.001 Å.

Section III

The annealing experiments demonstrate the role of high pressure in obtaining superconducting In_4SbTe_3 . These experiments also show that the superconductivity is not due to the presence of superconducting InTe(II) , the high-pressure rock-salt phase, in quantities too small to detect by x-ray diffraction. If this were the case, it would be unnecessary to anneal for long periods at elevated temperatures in order to eliminate superconductivity, since at atmospheric pressure InTe(II) is transformed to the nonsuperconducting low-pressure phase in a few minutes at only 135°C . Additional evidence that the superconductivity is not due to InTe(II) was obtained by experiments on mixtures containing low-pressure In_4SbTe_3 and 5 or 10 weight % InTe(II) . Both mixtures exhibited small superconducting transitions at 3.4°K , the transition temperature of pure InTe(II) , but no transition at 1.5°K , the transition temperature of high-pressure In_4SbTe_3 .

In initial experiments on the superconductivity of high-pressure InSb-InTe samples intermediate in composition between In_4SbTe_3 and InTe , data have been obtained for samples containing 80, 85, 90, and 95 mol % InTe . As expected, all four samples exhibited superconductivity. (It should be noted that low-pressure samples in this composition range, which contain In_4SbTe_3 saturated with InTe , do not exhibit superconductivity down to 1.3°K .) The transition temperature increased monotonically but not smoothly with increasing InTe content, since it increased quite sharply between 85 and 90 mol % InTe . This preliminary result suggests that the solubilities of InTe in In_4SbTe_3 and of InSb in InTe are considerably greater at high pressure than at low pressure, but that even at high pressure a complete series of solid solutions is not formed in the range between In_4SbTe_3 and InTe . Initial x-ray diffraction measurements have confirmed the increases in solubility at high pressure, but they have not established whether or not there is complete miscibility.

M. D. Banus Lynne B. Farrell
A. J. Strauss Muriel C. Plonko
Mary C. Finn

D. SUPERCONDUCTIVITY IN THE HIGH-PRESSURE $\text{InSb} - \beta\text{-Sn}$ SYSTEM

It was previously reported¹² that by alloying $\beta\text{-Sn}$ (body-centered tetragonal) with InSb_{II} (body-centered tetragonal),¹³ the superconducting transition temperature T_c of InSb_{II} is raised by more than 2°K . Samples containing 0.20 to 0.40 atom-fraction tin, annealed at 37 kbar for one hour at 300°C after melting and before quenching to room temperature, showed transitions at two different temperatures. The presence of two transitions in this composition range was attributed to a "quench effect" similar to the one observed in the two-phase region of the In-Sn system.¹⁴ On this basis, it was suggested that the $\text{InSb}_{\text{II}} - \beta\text{-Sn}$ system probably has a two-phase region between 0.05 and 0.65 atom-fraction tin even though complete solid solubility might be expected, since the terminal components have the same structures and very similar lattice constants.

A further study of the system has shown that attainment of equilibrium in the solid phase requires long periods of time as it does in the case of other similar systems, for example, Si-Ge (Ref. 15). When the annealing time at 37 kbar was increased from 1 to 20 or 40 hours, and the annealing temperature was increased from 300°C to between 320° and 350°C (increasing with increasing InSb concentration), the lower T_c was not observed while the single T_c increased to approximately 5°K in some alloys (Fig. III-7). These results suggest that a complete series of solid solutions is produced by prolonged annealing. With two phases present (nonequilibrium),

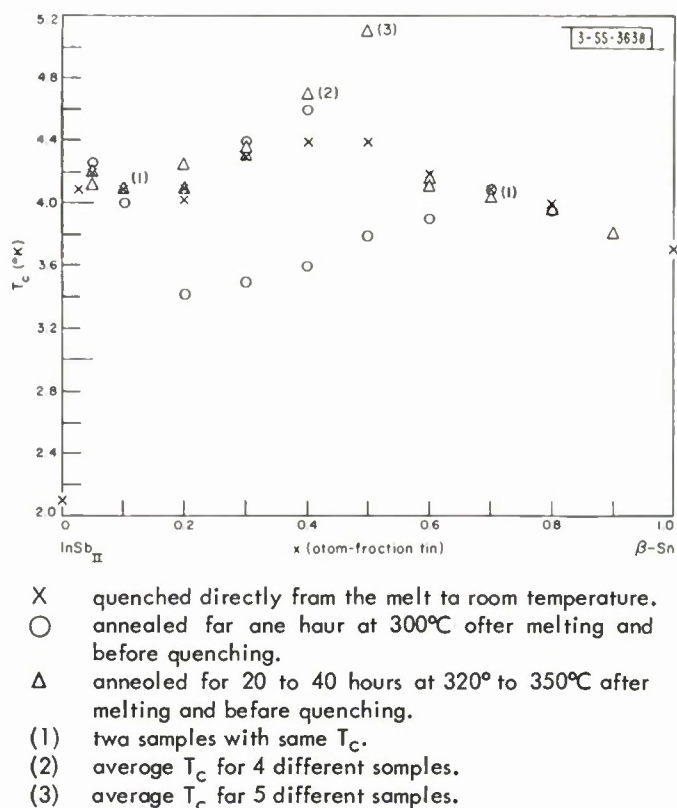


Fig. III-7. Superconducting transition temperature T_c vs nominal composition for $(\text{InSb}_{\text{II}})_{1-x}(\text{2Sn})_x$ alloys prepared at 37 kbar.

the lower T_c values are apparently due to the InSb_{II} -rich phase, whereas the upper T_c values are due to the Sn-rich phase. The latter were constant ($4.3 \pm 0.2^\circ\text{K}$) between 0.05 and 0.60 atom-fraction tin. Under equilibrium conditions in which only a single transition (presumably a single phase) was found, there is an unmistakable maximum at about 0.50 atom-fraction tin. This maximum may be associated with ordering of the alloy at 0.50 atom-fraction tin. In alloys containing less than 0.20 and more than 0.60 atom-fraction tin, the longer heat-treated samples gave the same T_c as samples heat-treated one hour or quenched directly, indicating the rapidity of equilibrium at these compositions.

In view of the present results, it is concluded that the $\text{InSb}_{\text{II}} - \beta\text{-Sn}$ system does not exhibit a two-phase region but exhibits complete solid solubility under equilibrium conditions.

Data on the temperature and time dependence of resistivity of $\text{InSb}_{\text{II}} - \beta\text{-Sn}$ alloys at atmospheric pressure show that at any temperature the rate of transformation to the stable low-pressure phases decreases monotonically with increasing tin content¹⁶ up to at least 0.6 atom-fraction tin, the highest tin content investigated. These data are therefore consistent with the formation of solid solutions in all proportions. In recent work, Darnell and Libby^{17,18} have also concluded from the variation of hardness, thermal stability, and superconducting transition

Section III

temperature on three alloys ($x = 0.33, 0.5, \text{ and } 0.56$) that InSb_{II} and tin are soluble in all proportions. However, these authors report that T_c increases monotonically from 2.1°K (InSb_{II}) to 3.7°K (Sn). Thus, except for the pure compounds, their T_c values are 0.5° to 1.9°K below those measured in our more detailed study.

M. D. Banus
Susan N. Vernon
H. C. Gatos

REFERENCES

1. W.D. Kingery, Property Measurements at High Temperatures (Wiley, New York, 1959).
2. Solid State Research Report, Lincoln Laboratory, M.I.T. (1963:3), p. 25, DDC 427340.
3. Solid State Research Report, Lincoln Laboratory, M.I.T. (1964:1), p. 37, DDC 601830.
4. Ibid., p. 31.
5. Solid State Research Report, Lincoln Laboratory, M.I.T. (1964:2), p. 39, DDC 606126.
6. B. Kubota and E. Hirota, J. Phys. Soc. Japan 16, 345 (1960).
7. J.B. Goodenough, Internat. Colloq. of CNRS on Oxygen Compounds of Transition Elements in the Solid State, Bordeaux (September 1964).
8. Solid State Research Report, Lincoln Laboratory, M.I.T. (1964:1), p. 34, DDC 601830.
9. N.A. Goryunova, S.I. Radautsan and G.A. Kiosse, Sov. Phys. Solid State 1, 1702 (1960).
10. I.P. Molodyan, S.I. Radautsan and I.A. Madan, Izv. Akad. Nauk Moldav. SSR, No. 10 (88), 91 (1961).
11. E.G. Grochowski, D.R. Mason, G.A. Schmitt and P.H. Smith, J. Phys. Chem. Solids 25, 551 (1964).
12. S.D. Nye, M.D. Banus and H.C. Gatos, J. Appl. Phys. 35, 1361 (1964).
13. M.D. Banus, R.E. Hanneman, A.N. Mariano, E.P. Warekois, H.C. Gatos and J.A. Kafalas, Appl. Phys. Letters 2, 35 (1963).
14. M.F. Merriam and M. vonHerzen, Phys. Rev. 131, 637 (1963).
15. C. Stohr and W. Klemm, Z. anorg. Chem. 241, 305 (1939).
16. M.D. Banus, L.B. Farrell and A.J. Strauss (to be published); Solid State Research Report, Lincoln Laboratory, M.I.T. (1964:2), p. 42, DDC 606126.
17. A.J. Darnell and W.F. Libby, Phys. Rev. 135, A1453 (1964).
18. B.R. Tittman, A.J. Darnell, H.E. Bömmel and W.F. Libby, Phys. Rev. 135, A1460 (1964).

IV. BAND STRUCTURE AND SPECTROSCOPY OF SOLIDS

A. INTERBAND TRANSITIONS IN ANTIMONY[†]

In addition to the oscillations in the magnetic field dependence of the reflectivity previously reported,¹ a new type of oscillatory behavior has been observed. Although, in the former case, the magnetic field associated with a particular oscillation in the reflectivity is independent of photon energy, the present phenomenon is strongly frequency dependent. The frequency-independent oscillations have been identified with an intraband optical deHaas-Shubnikov mechanism, whereas the frequency-dependent oscillations are identified with interband transitions. The identification of these new oscillations with cyclotron resonance is excluded for several reasons:

- (1) Such oscillations are energetically unfavorable since for $H \leq 10^5$ gauss, $\hbar\omega_c \lesssim 10^{-2}$ ev.
- (2) For certain fixed photon energies, the number of these oscillations exceeds the number of carrier types that have been previously reported.
- (3) As the magnetic field is decreased, the location of a given oscillation maximum shifts to lower photon energies and finally extrapolates to a finite energy gap.

Two sets of interband transitions have been observed. The interband transitions extrapolating to a bandgap of $\epsilon_g = 0.100 \pm 0.005$ ev have been observed with the magnetic field and Poynting vector of the light normal to all three principal crystallographic directions. In the case of the binary and bisectrix faces, these oscillations are enhanced by polarizing the light with E parallel to the trigonal direction. The perpendicular polarization emphasizes the second set of interband transitions for which $\epsilon_g = 0.15 \pm 0.01$ ev. These oscillations are expected to occur only for H normal to the binary and bisectrix faces and have, in fact, only been observed under these conditions. A recorder trace illustrating these oscillations with the magnetic field perpendicular to the binary face is shown in Fig. IV-1 for $\hbar\omega = 0.1968$ ev and the light polarized with E parallel to the bisectrix direction.

The observation of these interband transitions serves to explain certain puzzling features in both the magnetoplasma and optical deHaas-Shubnikov effects previously reported.^{1,2} In particular, neglecting the interband transitions led to the wrong sign for the magnetoplasma effect in the vicinity of $\hbar\omega \approx 0.10$ ev for H normal to the binary and bisectrix directions. Moreover, the free carrier model fails to predict the proper relationship between the amplitude of the magnetoplasma effect and its dependence on photon energy. Finally, a strongly frequency-dependent dielectric constant is needed to obtain the observed amplitude of the deHaas-Shubnikov effect and the dependence of this amplitude on photon energy.

A calculation of the magnetic field dependence of the optical reflectivity of antimony is in progress, which includes the interband transitions and the optical deHaas-Shubnikov effect.

[†] This experiment was performed using the high-field facilities of the M.I.T. National Magnet Laboratory.

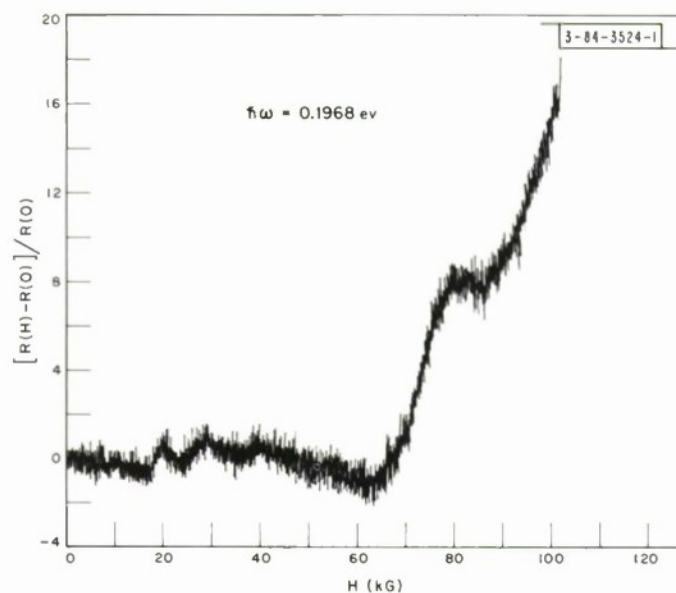


Fig. IV-1. Interband magnetorefectivity oscillations in antimony.
Photon energy $\hbar\omega = 0.1968$ eV and $T \approx 4^\circ\text{K}$.

The objective of this calculation is to construct a suitable model for the electronic band structure of antimony.

Mildred S. Dresselhaus
J. G. Mavroides

B. MAGNETIC SUSCEPTIBILITY IN GRAPHITE

Recent measurements by Williamson, *et al.*,³ of the magnetic susceptibility in single-crystal and pyrolytic graphite have confirmed the long-period oscillations first reported by Soule.⁴ Using the band parameters obtained from the magnetoreflexion experiment of Dresselhaus and Mavroides,⁵ the circular cross-sectional area of the Fermi surface about the zone corner has been computed, and the result is in agreement with the observed long-period oscillation.

At this point in the zone, there is neither an extremum in the cross-sectional area of the Fermi surface nor a stationary value of the cyclotron effective mass, but there is a twofold degeneracy of the energy levels. A calculation of the temperature dependence of the magnetic susceptibility in the low-field limit is in progress to determine (1) whether deHaas-vanAlphen oscillations can occur at such a point in the zone, (2) the relation between the temperature dependence of χ and the effective mass, and (3) the anisotropy effect which is observed as the magnetic field is rotated from the c-axis to an a-axis.

Mildred S. Dresselhaus
G. F. Dresselhaus

C. ALFVÉN WAVES IN GRAPHITE

Oscillations in the microwave transmission of single-crystal and pyrolytic graphite have been recently observed by Surma, Furdyna and Praddaude⁶ and have been attributed to Alfvén wave propagation through thin samples. For semimetals with simple parabolic bands, the

velocity of propagation v of these waves depends on the carrier density n_i and effective mass m_i^* of the holes and electrons through the relation⁷

$$v^2 = \frac{H^2}{4\pi} (n_e m_e^* + n_h m_h^*)^{-1} \quad (1)$$

in which H is the magnetic field. In the case of graphite, both the density of states and the cyclotron effective mass depend on the wave vector k_z . By using the band parameters obtained from the magnetoreflexion experiment of Dresselhaus and Mavroides,⁵ the products $n_e m_e^*$ and $n_h m_h^*$ have been calculated by suitable integration over k_z . Neglecting trigonal warping of the Fermi surface, the values obtained are $n_e m_e^* = 1.38 \times 10^{-10} \text{ g/cm}^3$ and $n_h m_h^* = 1.84 \times 10^{-10} \text{ g/cm}^3$, in good agreement with the experimental observation.⁶ The effect of trigonal warping ($\gamma_3 \neq 0$) on the Alfvén wave propagation is also being studied.

In order to obtain the line shape for the transmission experiment,⁶ the expression for the high-frequency conductivity in a magnetic field is being evaluated for the graphite band parameters.⁵ The conductivity is used to calculate quantitatively the transmission of microwave power through a single crystal of material. Both cyclotron resonance and Alfvén wave behavior are obtained.

Mildred S. Dresselhaus
G. F. Dresselhaus

D. REFLECTIVITY OF Mg_2Si , Mg_2Ge , AND Mg_2Sn

The reflectivity of Mg_2Si , Mg_2Ge , and Mg_2Sn has been measured in the 1- to 11-ev photon energy range. The measurements below 2 ev were made at 300°K, and those from 2 to 11 ev were made at 77°K. These II-IV compounds are all semiconductors which crystallize in the anti-fluorite structure. The reflectivity, as shown in Fig. IV-2, is very similar to materials of zinc-blende structure such as the III-V compounds.

A Kramers-Krönig analysis is being performed on the data to determine the real and imaginary parts of the dielectric constant. This will facilitate an interpretation based on Lee's published band-structure calculations.⁸ A comparison of these calculations with other experimental evidence concerning phototreshold measurements⁹ shows that theoretical energy values for the indirect and direct energy gap in Mg_2Si and Mg_2Ge are in error by about 1 ev. Reasonable interpretation of the reflectivity spectra will require careful adjustment of the calculations to fit the complex dielectric constant derived from the Kramers-Krönig analysis.

W. J. Scouler

E. BAND STRUCTURE OF HgTe AND HgTe-CdTe ALLOYS

The gray tin band model of Groves and Paul,¹⁰ extended to include overlap of the valence and conduction bands, has been applied to HgTe and $\text{Cd}_x\text{Hg}_{1-x}\text{Te}$ alloys. This model is consistent with the systematics of III-V and II-VI compounds with zinc-blende structure and with all available experimental data. It accounts for the semimetallic nature of those alloys for which $x < 0.20$. In this model, the direct energy gap at $k = 0$, $E_1(x) \equiv E_{\Gamma_6(\Gamma_1)} - E_{\Gamma_8(\Gamma_{15})}$, is a nearly linear function of lattice constant, and negative for $x < 0.17$, as shown in Fig. IV-3. The highest valence band edge E_v lies above $E_{\Gamma_8(\Gamma_{15})}$ by an energy E_2 of 0.01 to 0.04 ev for $x \leq 0.20$.

Section IV

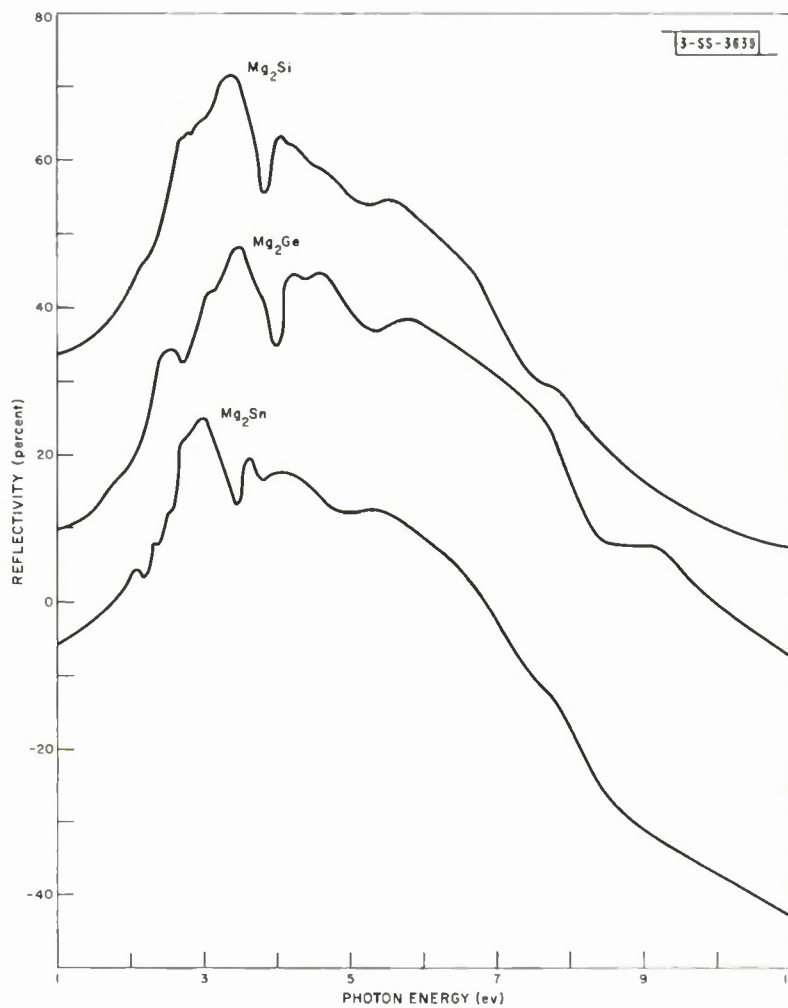
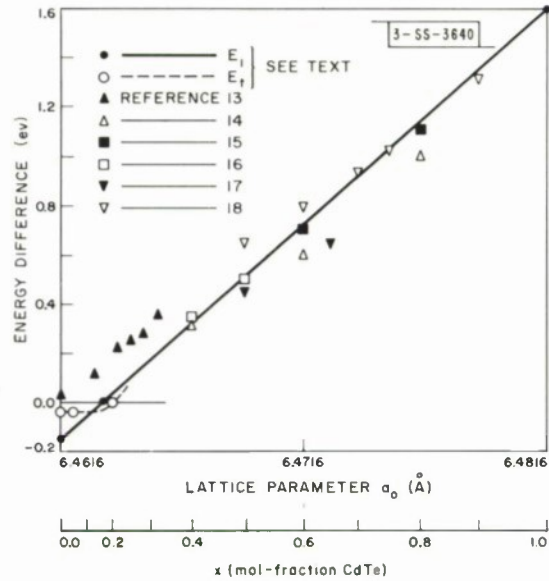


Fig. IV-2. Reflectivity of Mg_2Si , Mg_2Ge , and Mg_2Sn from 1 to 11 eV. Data below 2 eV were taken at 300°K and those above 2 eV, at 77°K. The ordinate refers to Mg_2Si . Each of the other curves are displaced 25 percent downward from one another.

Fig. IV-3. Variation of E_1 and E_t with lattice parameter a_0 and with composition x in alloy system $\text{Cd}_x\text{Hg}_{1-x}\text{Te}$. Data points, except those discussed in text and those listed in Ref. 13, are from our interpretation of published results of optical transmission measurements at zero magnetic field.



As the mean atomic number $Z_{\text{Cd}}x + Z_{\text{Hg}}(1-x) = 48x + 80(1-x)$ increases, the energy of the $\Gamma_6(\Gamma_1)$ Bloch function, which has a $\text{Cd}_x\text{Hg}_{1-x}$ s-like character, is expected to be lowered more than that of the $\Gamma_8(\Gamma_{15})$ Bloch function, which has a tellurium p-like character. From this, one predicts that $E_1(0)$ is less than $E_1(1)$, in agreement with observation (Fig. IV-3). Since the Γ_6 and Γ_8 levels have different symmetry, they move independently as the potential changes with alloying and should not exhibit any unusual behavior near the composition where they become degenerate. This picture suggests that E_1 varies smoothly and monotonically with alloying as assumed in the model.

In constructing Fig. IV-3, we have used for $E_1(x)$ the values $E_1(1) = 1.6$ eV (Ref. 11), $E_1(0.17) = 0.006 \pm 0.006$ eV, and $E_1(0) = -0.14 \pm 0.05$ eV. The value for $x = 0.17$ is obtained from analysis of cyclotron resonance transitions in magnetorefectivity data.¹² The very small value of the observed cyclotron resonance mass at $x = 0.17$, $m^* = 0.003 m_0$, is direct evidence for a small gap. The magnitude of the value for $E_1(0)$ was deduced from the variation of the effective mass m^* with carrier concentration N . The sign of $E_1(0)$ was chosen negative, because $E_1(x)$ would not be monotonic for $E_1(0)$ positive. A positive value of $E_1(0)$ can also be ruled out if $E_1(x)$ is assumed to be a smooth, but not necessarily monotonic, function of x , since $E_1(0) > 0$ is inconsistent with a small E_2 for the range $0 \leq x \leq 0.2$.

Symmetry and continuity arguments show that for the zinc-blende structure, a Γ_8 level cannot be the valence band edge, so that E_v must lie above the valence band Γ_8 level. Our model for the band structure of $\text{Cd}_x\text{Hg}_{1-x}\text{Te}$, which is illustrated in Fig. IV-4 for several values of x , provides for $E_v > E_{\Gamma_8(\Gamma_{15})}$ and the variation of E_1 with x shown in Fig. IV-3 (see also Refs. 13-18). According to this model, the alloy is a semimetal when $E_1 \leq E_2$.

Semimetallic behavior in $\text{Cd}_x\text{Hg}_{1-x}\text{Te}$ has been confirmed by new data which, for $x < 0.20$, lead to the negative values given in Table IV-1 for the thermal gap $E_t(x) \equiv E_c - E_v$, where E_c is the lowest conduction band edge. The value $E_t(0) = -0.02 \pm 0.01$ eV was obtained by detailed analysis of the variation in Hall coefficient between 4° and 300°K for various extrinsic n-type

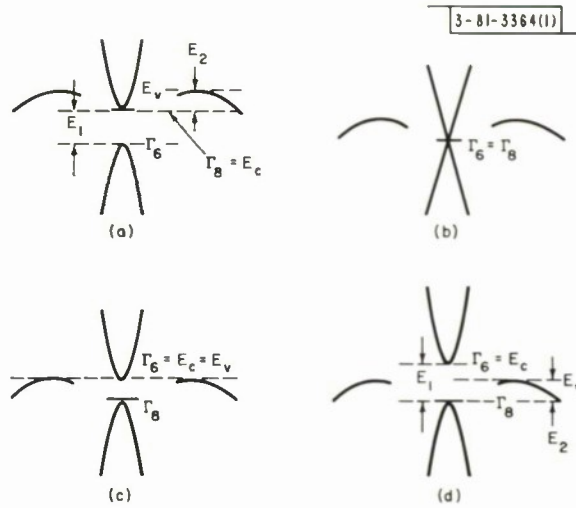


Fig. IV-4. Schematic diagrams of proposed band structures of $\text{Cd}_x\text{Hg}_{1-x}\text{Te}$ alloy system for key values of composition x . (a) $x = 0$, semimetal with $E_1 \cong -0.14$ eV and $E_t = -E_2 = -0.02$ eV. (b) $x = 0.17$, semimetal with $E_1 \cong 0$ and $E_t = -E_2 \cong -0.02$ eV. (c) $x = 0.20$, semimetal-semiconductor transition composition with $E_1 = E_2 \cong 0.03$ eV and $E_t \cong 0.0$ eV. (d) $x > 0.20$, semiconductor, $E_t > 0$. (Our model of valence band structure pertains only to energies in vicinity of valence band edges.)

TABLE IV-1 SUMMARY OF SALIENT BAND PARAMETERS FOR $\text{Cd}_x\text{Hg}_{1-x}\text{Te}$					
All energies are in meV. $E_1 \equiv E_{\Gamma_6(\Gamma_1)} - E_{\Gamma_8(\Gamma_{15})}$; $E_2 \equiv E_v - E_{\Gamma_8(\Gamma_{15})}$; $E_t \equiv E_c - E_v$.					
x	E_1	E_t	E_2	$\frac{m_e^*(k=0)}{m_0}$	$\frac{m_h^*}{m_0}$
0	$-140 \pm 50^{a,b,c}$	-20 ± 10^d	20 ± 10^d	$0.02^{a,b}$	—
0.05	-100^c	$-20 \pm 10^{e,c}$	$20 \pm 10^{e,c}$	$0.009^{b,c}$	$0.3^{e,c,b}$
0.17	6 ± 6^a	—	—	$0.0006^{o,b}$	—
0.20	$+35 \pm 5^c$	$2 \pm 2^{e,c}$	$33 \pm 6^{e,c}$	$0.0035^{b,c}$	—
1.0	1600^a	—	—	$0.1^{a,b}$	—

a From infrared measurements.

b Used conduction band $E(k)$ derived from $\vec{k} \cdot \vec{p}$ approach.

c From E_1 vs x (Fig. IV-3).

d From $R(1/T)$ data.

e From magneto-Hall data.

samples. For $x = 0.05$ and $x = 0.20$, p-type samples have been found for which the Hall coefficient R at 4.2°K changes from a negative value to a positive saturation value as the magnetic field increases from 0.1 to 5 kG. Detailed analysis of the mixed conduction results has yielded values of the electron and hole carrier concentrations. From these results, along with $E_1(x)$ from Fig. IV-3, the other values of E_t shown in Table IV-1 were obtained.

This work has been accepted for publication in Solid State Communications.

T. C. Harman	J. G. Mavroides
W. H. Kleiner	J. M. Honig
A. J. Strauss	D. H. Dickey
G. B. Wright	

F. BAND STRUCTURE OF GADOLINIUM METAL

An augmented plane-wave calculation¹⁹ has been performed to obtain the approximate non-relativistic energy bands in gadolinium metal. The preliminary results indicate that these bands differ markedly from those of free electrons. This is principally due to the fact that the bands originating from atomic 5d and 6s states overlap and are strongly mixed. This situation is similar to that which occurs in transition metals.

J. O. Dimmock
A. J. Freeman[†]
R. E. Watson[‡]

G. THEORY OF THE "COLLISION DRAG" EFFECT IN ULTRASONIC ABSORPTION IN METALS

In the theory of ultrasonic absorption in metals, the details of collision processes with thermal phonons or impurities are of fundamental importance. The primary difference between the absorption of electromagnetic and ultrasonic waves in a metal is that the former drives only the electrons, whereas the ultrasonic wave drives, in addition, the scattering "centers," whether they are local impurities or thermal phonons. In the description of the relaxation processes of the electrons, these effects have been designated as the collision drag effect. Specifically, it is assumed that the electrons relax not to a thermal equilibrium distribution, but to one with mean velocity equal to the local velocity impressed by the sound wave.

This effect has been studied theoretically by Holstein²⁰ for the case of scattering by thermal phonons and by Nagaoka²¹ for static impurity scattering. These authors used different methods and considered only special situations with respect to the wavelength of the acoustic wave; e.g., Holstein used a wave-packet description of the collision process, whereas Nagaoka used a perturbation expansion, valid only for wavelengths shorter than the mean free path.

We have studied this effect on the basis of the transport theories for inhomogeneous driving fields previously presented by the author.²² We have developed the corresponding transport equations for both phonon and impurity scattering for arbitrary wavelengths of the acoustic wave. In certain limits, we prove that the collision drag effect may be described as above. The treatment is rigorous, except that the Born approximation was used for the scattering interactions. Thus, the treatment complements and generalizes the previous theories on this topic. A detailed account of the work will be presented in a separate report.

P. N. Argyres

[†] National Magnet Laboratory.

[‡] Bell Telephone Laboratories.

H. ELASTOTRANSPORT PROPERTIES OF MATERIALS

A systematic, formal treatment of elastotransport theory has been provided for one-carrier semiconductors or metals in the absence of magnetic fields. This theory takes into account not only the deformation potential model which has been adequately treated in the past,²³ but also the effect of strain on the effective mass tensors, intravalley scattering, and Fermi level. Explicit formulas for the piezoresistivity, piezo-Seebeck coefficient, and the electronic component of the piezothermal conductivity have been derived for sets of ellipsoids oriented along the $\langle 100 \rangle$, $\langle 110 \rangle$, and $\langle 111 \rangle$ axes in momentum space, in terms of Fermi-Dirac statistics. The theory, which is linear in the strain, is based on the Boltzmann transport equation in the relaxation time approximation, assuming a quadratic dependence of energy on wave-number vector.

The work will be submitted shortly for publication.

W. H. Kleiner
J. M. Honig
Lorella M. Jones

I. ELASTIC CONSTANTS OF HgTe

The room-temperature elastic constants of HgTe have been measured by means of the ultrasonic pulse technique. In units of 10^{11} dynes/cm², it is found that $c_{11} = 5.08$, $c_{12} = 3.58$, and $c_{44} = 2.05$. Using these values and the Szigeti relation²⁴ specialized to the zinc-blende structure for the fundamental lattice absorption frequency ω_o , namely,

$$\omega_o^2 = 4a_o \left(\frac{\epsilon + 2}{\epsilon_o + 2} \right) \frac{K}{M} \quad (1)$$

where a_o is the lattice constant, $K = (c_{11} + 2c_{12})/3$, M is the reduced mass per ion pair, and ϵ_o and ϵ are the static and high-frequency dielectric constants, respectively, a value of $\omega_o = 2.42 \times 10^{13}$ is calculated. This value is in reasonable agreement with the experimental absorption frequency²⁵ $\omega_o = 2.20 \times 10^{13}$ considering that the Cauchy relation, $c_{12} = c_{44}$, does not hold in HgTe.

By suitably averaging the velocities over possible propagation directions, a Debye characteristic temperature Θ can be calculated from the elastic data. Using the technique worked out by deLaunay,²⁶ and neglecting the small temperature variation of the constants, a Debye characteristic temperature at absolute zero, $\Theta_o = 105^\circ\text{K}$, is calculated.

J. G. Mavroides
D. F. Kolesar

J. PLASMA WAVE TRANSMISSION THROUGH BISMUTH

A theoretical and experimental study has been made of wave transmission through degenerate hole-electron plasmas in solids, emphasizing the weakly transmitted waves which have not been previously examined in detail. Transmission experiments allow the separation of weakly excited, lightly damped waves from strongly excited, heavily damped ones. An experimental technique to accomplish this has already been described,²⁷ which uses a very sensitive receiver capable of measuring phase or group velocity of transmitted signals attenuated up to 200 db.

Two of the weakly transmitted waves studied were the resonance-damped Alfvén wave and the "branch cut" wave, which is a superposition of single-particle excitations. The Alfvén wave

occurs in a plasma composed of equal densities of oppositely charged carriers. In the limits of high magnetic field and negligible collision rate, this wave is strongly transmitted with a propagation constant q given by

$$q = \frac{\omega(\mu_o n)^{1/2} (m_1 + m_2)^{1/2}}{B_o} \quad (2)$$

where n is the carrier density, m_1 and m_2 are the carrier masses, and B_o is the magnetic field. However, when the magnetic field is reduced enough so that the wave phase velocity v_p falls below the Fermi velocity v_F of either carrier, the wave becomes strongly resonance-damped, and the propagation constant becomes independent of B_o to first order in v_p/v_F .

The amplitude and phase delay of a signal transmitted at 8.8 Gcps and 4.2°K along the trigonal axis through an 83- μ -thick slab of bismuth are shown as a function of DC magnetic field in Fig. IV-5(a) and (b), respectively. In this geometry, $\omega_c > \omega$ for both holes and electrons when $B_o > 250$ gauss. However, the Alfvén phase velocity is greater than the electron Fermi velocity (about 7×10^7 cm/sec along the trigonal axis in bismuth), only for B_o greater than about 1250 gauss; hence for $B_o < 1250$ gauss, the wave will be resonance-damped. As seen in Fig. IV-5, both the phase and amplitude of the transmitted signal as a function of B_o^{-1} are less dependent on B_o for B_o less than about 1250 gauss.

The calculation of the electric field excited in a semi-infinite medium by an incident electromagnetic wave involves integration around the various singularities of the complex dielectric constant in the q -plane. Mathematically, the Alfvén wave arises from a pole, but in addition there are branch-point singularities in the dielectric constant. When B_o is small enough for resonance damping to occur, the contributions to the electric field from integration along the branch cuts are comparable to the residue of the pole. In this case, the electric field does not

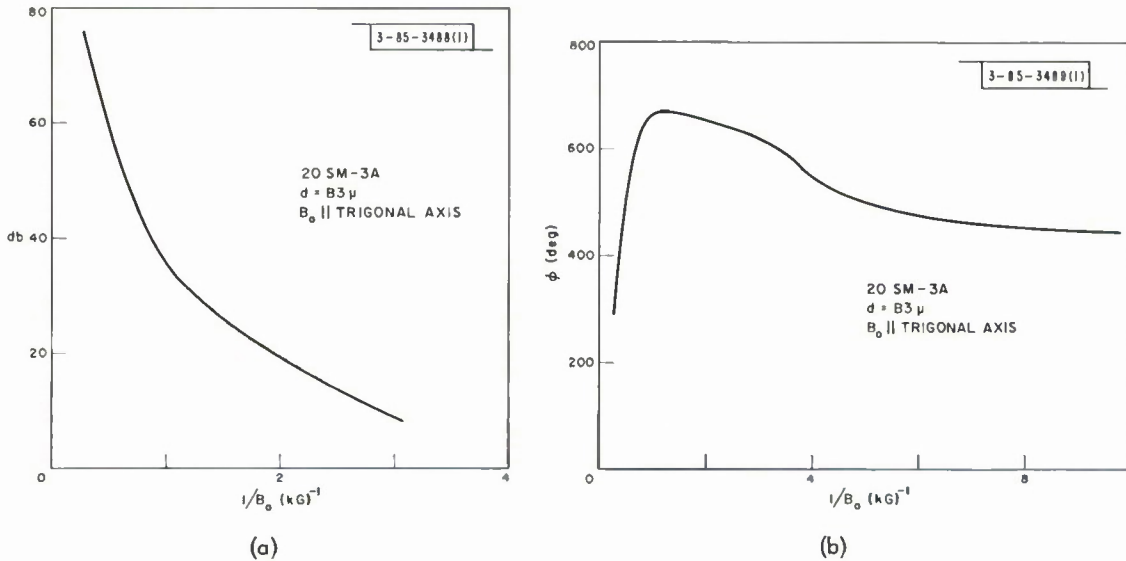


Fig. IV-5. (a) Amplitude of signal transmitted through an 83- μ -thick slab of bismuth at 4.2°K and 8.8 Gcps as a function of magnetic field. (b) Phase of signal transmitted through an 83- μ -thick slab of bismuth at 4.2°K and 8.8 Gcps as a function of magnetic field.

Section IV

vary as $\exp[-iqz]$ and no simple analytic expression exists. Numerical computation is now under way to determine the electric field as a function of B_0 .

At zero magnetic field, the branch cut integration for a one-component plasma can be evaluated asymptotically²⁸ to yield for the electric field at depths greater than several mean free paths

$$E(z) = -A \frac{v_F^2}{\omega_p^2} \frac{\exp[-(\nu + i\omega) z/v_F]}{z^2} \quad (3)$$

where A is a constant involving the strength of excitation, and ν is the collision frequency. Measurements at X-band frequencies on several 50- to 100- μ -thick bismuth slabs have yielded values of about 7×10^7 cm/sec for the phase and group velocities of signals transmitted along the trigonal axis at zero magnetic field. These velocities are just equal to the electron Fermi velocity, in agreement with the above expression evaluated for the electron branch cut. In the quantum mechanical expression for the dielectric constant, the branch cut actually becomes a line of closely spaced poles, each pole corresponding to a dressed single-particle excitation. These excitations are the transverse analogs to the longitudinal vanKampen^{29,30} modes.

W. G. May
A. L. McWhorter

REFERENCES

1. Solid State Research Report, Lincoln Laboratory, M.I.T. (1964:2), p. 51, DDC 606126.
2. Solid State Research Report, Lincoln Laboratory, M.I.T. (1964:1), p. 42, DDC 601830.
3. S.J. Williamson, S. Foner and M.S. Dresselhaus, Proc. of the 9th Internat. Conf. on Low Temperature Physics, Columbus, Ohio (1964) (to be published).
4. D.E. Soule, IBM J. Research Develop. 8, 268 (1964).
5. M.S. Dresselhaus and J.G. Mavroides, IBM J. Research Develop. 8, 262 (1964).
6. M. Surma, J.K. Furdyna and H. Praddaude (to be published).
7. G.A. Williams and G.E. Smith, IBM J. Research Develop. 8, 276 (1964).
8. P.M. Lee, Phys. Rev. 135, A1110 (1964).
9. C.A. Mead, J. Appl. Phys. 35, 2460 (1964).
10. S. Groves and W. Paul, Phys. Rev. Letters 11, 194 (1963).
11. D.G. Thomas, J. Appl. Phys. 32, 2298S (1961).
12. A.J. Strauss, T.C. Harman, J.G. Mavroides, D.H. Dickey and M.S. Dresselhaus, Proc. of the Internat. Conf. on the Physics of Semiconductors, Exeter (1962), p. 703.
13. M.D. Blue, Phys. Rev. 134, A226 (1964). In view of the difficulties in preparing undamaged samples and the variety of types of contributions to the absorption coefficient to be expected for the model of Fig. IV-3, we feel that deductions made to date from optical absorption data regarding optical gap energies less than a few tenths of an electron volt are inconclusive. Our deductions of $E_1(0)$ and $E_1(0.17)$ depend on reflectivity experiments in the frequency region dominated by free-carrier effects, and hence do not suffer from the above difficulties of interpretation.
14. W.D. Lawson, S. Nielson, E.H. Putley and A.S. Young, J. Phys. Chem. Solids 9, 325 (1959).
15. M.V. Kot, V.G. Tyrziu, A.V. Simashkevich, Yu. Yl. Maronchuk and V.A. Mshensky, Fiz. Tver. Tela. 4, 1535 (1962) [translation: Soviet Phys. - Solid State 4, 1128 (1962)].
16. F. Bailly, G. Cohen-Solal and Y. Marfaing, C.R. Acad. Sci, Paris 257, 102 (1963).
17. V.I. Kvanov-Omsky, B.T. Kolomiets and A.A. Malkova, Fiz. Tver. Tela. 6, 1457 (1964).
18. A.D. Schneider and I.S. Zhurko, Ukrainian J. Phys. 9, 32 (1964).
19. J.C. Slater, Phys. Rev. 92, 1126 (1953).
20. T. Holstein, Phys. Rev. 113, 479 (1959).
21. Y. Nagaoka, Progr. Theoret. Phys. 26, 589 (1961).
22. P.N. Argyres, Phys. Rev. 132, 1527 (1963); Solid State Research Report, Lincoln Laboratory, M.I.T. (1963:4), p. 49, DDC 435023.
23. R.W. Keyes, Solid State Physics, Vol. 11, F. Seitz and D. Turnbull, eds. (Academic Press, New York, 1960), p. 149.
24. B. Szigeti, Proc. Roy. Soc. A204, 51 (1950).
25. D.H. Dickey and J.G. Mavroides, Solid State Comm. 2, 213 (1964).
26. J. deLaunay, Solid State Physics, Vol. 2, F. Seitz and D. Turnbull, eds. (Academic Press, New York, 1956), p. 219.
27. A.L. McWhorter and W.G. May, IBM J. Research and Develop. 8, 285 (1964).
28. G.E.H. Reuter and E.H. Sondheimer, Proc. Roy. Soc. A195, 336 (1948).
29. N.G. vanKampen, Physica 21, 949 (1955).
30. _____, Physica 23, 641 (1957).

V. MAGNETISM AND RESONANCE

A. MAGNETIC ORDERING

1. On the Determination of Magnetic Ordering from High-Temperature Expansions

During this quarter, we have undertaken an initial investigation of a class of functions $\varphi(c, T) = N^{-1} \sum_{nm} c_n^* c_m \langle \vec{S}_n \cdot \vec{S}_m \rangle_T$, where N is the number of sites, c is a set of complex numbers, c_n satisfying $\sum_n |c_n|^2 = N$, and $\langle \vec{S}_n \cdot \vec{S}_m \rangle_T$ is the static correlation function between spins at sites \vec{R}_n and \vec{R}_m . We have argued that if the set $c^{(o)}$ maximizes $\varphi(c, T)$, then $\varphi[c^{(o)}(T), T] \rightarrow \infty$ as $T \rightarrow T_c$, the critical ordering temperature, whereas $\varphi[c(T), T]$ is bounded as $T \rightarrow T_c$ for $c(T)$ orthogonal to $c^{(o)}(T)$. Thus a divergence to infinity of $\varphi[c^{(o)}(T), T]$ indicates the location of T_c , and the form of $c^{(o)}(T_c)$ contains information about the type of order. For example, ferromagnetic ordering is predicted for $c_n^{(o)}(T_c) = 1$, and a sinusoidal or spiral ordering of wave vector \vec{k}_0 is predicted for $c_n^{(o)}(T_c) = \exp[i\vec{k}_0 \cdot \vec{R}_n]$. We have estimated $c^{(o)}(T)$ from a finite number of terms in the expansion of $\varphi(c, T)$ in powers of $1/T$ for several types of Heisenberg magnets. The results, particularly interesting for spinels, will be discussed in a future report.

T. A. Kaplan K. Dwight, Jr.
H. E. Stanley N. Menyuk

2. Ferrimagnetic Resonance in Chromium Spinel

a. MnCr_2O_4

Measurements of magnetic resonance as a function of temperature were made on powder samples¹ of ferrimagnetic MnCr_2O_4 at 35 kMcps. At room temperature, a single resonance having a line width $\Delta H = 500$ gauss and $g_{\text{eff}} = 2.02$ was observed. Upon cooling the sample to liquid helium temperatures, the resonance broadened and the line width increased to 1200 gauss. Two small additional resonances superimposed on the main resonance were detected at 13° to 15°K and increased in intensity with further decrease in temperature. The appearance of these satellite resonances at low temperatures may be associated with the break in the magnetization occurring at 18°K, which is attributed to a collinear \rightarrow defined spiral magnetic transition.²

b. CoCr_2S_4

The magnetic resonance of CoCr_2S_4 powder¹ was studied as a function of temperature at 35 kMcps. A single resonance was observed as the sample was cooled below the Néel temperature of 240°K. The peak resonance absorption increased with decreasing temperature proportional to the sample magnetization. Below 224°K, the resonance split into a high-field strong resonance and a low-field weaker resonance, with the separation between peaks increasing to 2 kG at 180°K. Further decrease to liquid helium temperatures caused a shift of the resonance peaks toward lower fields by an amount of 2 kG. The origin of the splitting is not clear. It is not likely that it is associated with spiral ordering, since neutron diffraction results are

Section V

consistent with Néel ordering.³ It is possibly a result of powder samples that cause averaging over the anisotropy of the material.

c. MnCr_2S_4

Measurements of magnet resonance as a function of temperature have been made on MnCr_2S_4 (Ref. 1) powder at 33.2 kMcps. Above 80°K, a resonance having a line width $\Delta H = 200$ gauss and $g_{\text{eff}} = 2.06$ was observed. As the temperature was decreased below 80°K, the line width broadened and at 20°K, $\Delta H = 1000$ gauss. Two small additional resonances appeared at 14°K, and increased in intensity as the temperature was lowered. These small resonances were situated at about 800 gauss on each side of the main peak. The integrated resonance absorption was also measured as a function of temperature and, above 20°K, was found to be closely proportional to the sample magnetization. Again, the origin of the splitting is not clear, since neutron diffraction is consistent with Néel ordering.³

J. J. Stickler
H. J. Zeiger

B. MODIFICATION OF LIGAND-FIELD THEORY FOR THIOSPINELS

In the last Solid State Research Report,⁴ it was pointed out that metallic conductivity in the oxides is due to a breakdown of the ligand-field theory, either as a result of cation-cation covalence or as a result of cation-anion covalence. It was also reported that LaNiO_3 is metallic and Pauli paramagnetic, which indicates that in this 3d-transition-metal oxide the cationic orbitals directed toward the nearest-neighbor anions have been transformed from localized-electron to σ^* -band states by cation-anion covalence. The metallic conductivity and Pauli paramagnetism of LaTiO_3 indicates that even the π -bonding orbitals of this 3d-transition-metal oxide are transformed into π^* -band states. Since the sulfides are more covalent than the oxides, it is natural to anticipate that the transformation of anion-directed cationic 3d orbitals into anti-bonding σ^* -band states will be even more prevalent. To test this idea, two sets of schematic energy-level diagrams for the thiospinels have been constructed with the assumptions of (1) ligand-field theory, and (2) σ^* -band formation. These two models lead to different qualitative predictions for the magnetic and electric properties of several thiospinels. These predictions were compared with recent unpublished data⁵ on the thiospinels, and it is found that the prediction from the σ^* -band model, in contrast to those from the ligand-field model, are in essential agreement with the data. However, the existence of a Jahn-Teller effect in CrS and the properties of MnS indicate that when there are four or five unpaired spins per cation, intra-atomic exchange may be strong enough to stabilize localized ligand-field states rather than σ^* -band states.

J. B. Goodenough

C. SINGLE-CRYSTAL GROWTH

Several programs of crystal growth of various materials have been continued. A brief summary of some of these in which progress has been made is given below.

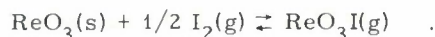
1. Vanadium Spinels

It has been previously pointed out⁶ that reduction of pentavalent vanadium in the presence of Co^{+2} leads to the precipitation of $\text{Co}_{1+\delta}\text{V}_{2-\delta}\text{O}_4$ from fluxes of $\text{Na}_2\text{WO}_4\text{-WO}_3$. By carrying out the reduction electrolytically, crystals up to a centimeter in diameter have been grown.⁴ Variation of the experimental conditions, such as flux composition and temperature, provides a means of varying the parameter δ . Thus far, δ has been varied only in the limits $0.11 < \delta < 0.54$. Several attempts have been made to reduce δ to zero without success. In view of the difficulty of preparing CoV_2O_4 ($\delta = 0$) even as polycrystalline powders by ceramic techniques,^{7,8} an extension of this investigation is being made to the system $\text{Mg}_{1+\delta}\text{V}_{2-\delta}\text{O}_4$. In the latter system, the end member MgV_2O_4 is expected to be considerably more stable, and all valence problems associated with the A-site ion are alleviated.

2. Rhenium Trioxide

As shown in the previous Solid State Research Report,⁴ the preparation of stoichiometric ReO_3 is a formidable problem. The usual preparative techniques tend to yield products that deviate from their theoretical reducing power by several percent. We have found that these products can be purified, however, by vapor transport in a two-zone furnace using iodine as the transporter. Since ReO_3 disproportionates into ReO_2 and Re_2O_7 at about 400°C , it was necessary to effect transport below this temperature. Under conditions of high iodine vapor pressure (an excess of iodine was used so that liquid iodine was always in equilibrium with its vapor), transport of ReO_3 occurred in the direction of the cooler zone. Optimum temperature of the reaction chamber (hot zone) appeared to be in the 360° to 380°C range.

Chemical principles underlying vapor transport reactions have been discussed by Schafer, *et al.*,⁹ and by Nitsche, *et al.*¹⁰ Such reactions are based on the chemical equilibrium established in a closed system between a solid phase and gaseous components. If the equilibrium is disturbed locally (e.g., by imposing a temperature gradient on the vessel containing the system), transport of the solid phase may occur. For the transport of ReO_3 , a number of possible reaction mechanisms exist, the most probable of which involves the formation of a rhenium oxyiodide. Perhaps the simplest of these possibilities is the reaction



The direction of transport indicates that the equilibrium constant for formation of the volatile complex increases with increasing temperature over the experimental range of T . Thus, the reaction is endothermic.

These observations immediately suggest application of the transport technique to growth of ReO_3 single crystals. Since ReO_3 disproportionates without melting at a low temperature, usual crystal growth techniques from the melt cannot be applied. In several preliminary experiments, we have obtained numerous bronze-red single crystals of ReO_3 that possess a cubic habit. Maximum size of these crystals has been from 1 to 2 mm on an edge. Optimum gradient conditions seem to be those for which the crystallization chamber is about 5°C below that of the reaction chamber.

3. Yttrium Aluminum Garnet and Indium Vanadate

The garnet $\text{Y}_3\text{Al}_5\text{G}_{12}$ and InVO_4 are of interest as laser materials. Crystal growth of these materials from the melt is difficult because of the high melting point of the former and decomposition of the latter before melting. Preliminary experiments have been made to determine the feasibility of growing these materials from fluxes of polytungstate and V_2O_5 , respectively. Results of these experiments indicate good crystallization of the desired products, and attempts to grow large single crystals are in progress.

D. B. Rogers
E. J. Delaney
A. Ferretti

D. PREPARATION AND SUSCEPTIBILITY OF RARE-EARTH TRIFLUORIDES AND OXYFLUORIDES

As a first step toward the preparation and investigation of the magnetic properties of the rare-earth oxyfluorides, we have prepared several of the rare-earth trifluorides and measured their magnetic susceptibilities from helium to room temperature. The trifluorides exist in either a simple hexagonal or a complex rhombohedral structure.

The results for the members of the series prepared thus far are given below:

	μ_{th}	μ_{exp}	Θ
CeF_3	2.54	2.47	49.8
GdF_3	7.94	7.79	-4.1
TbF_3	9.72	9.47	0.2
DyF_3	10.65	10.42	0.1
HoF_3	10.61	10.47	9.7
ErF_3	9.58	9.34	10.7
NdF_3	3.62	3.60	50.0

The close agreement of the theoretical free-ion magnetic moments μ_{th} and the experimental μ_{exp} (in Bohr magnetons) and the small Weiss constants Θ [in degrees Kelvin, where $\chi_m = C_m/(T + \Theta)$] not only indicates the purity of the materials but also small crystal field splittings. There was no evidence of magnetic order above 4°K.

P. M. Raccach
S. Kern
B. Feldman

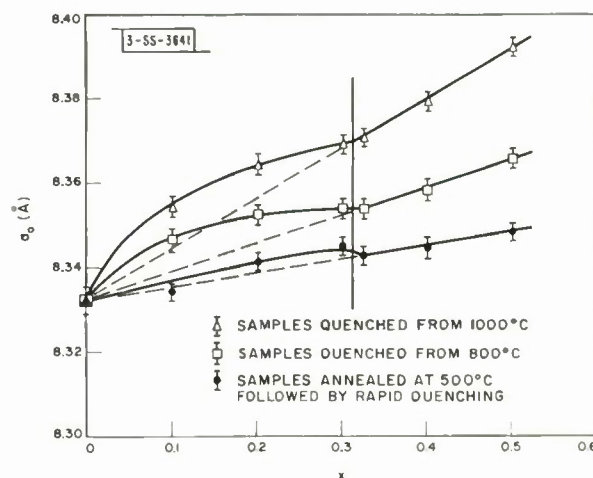
E. EFFECT OF Mn^{+3} ON THE CRYSTAL CHEMISTRY OF SOME LITHIUM SPINELS

Interest in the effect of the Jahn-Teller ion Mn^{+3} on cation ordering in lithium spinels has been indicated in previous Solid State Research Reports.^{6,4} It was shown that only 13 to 15 percent Mn^{+3} on the octahedral sites of the spinel systems $\text{Li}_{0.5}\text{Ga}_{2.5-x}\text{Mn}_x^{+3}\text{O}_4$ and $\text{Li}_{0.5}\text{Fe}_{2.5-x}\text{Mn}_x^{+3}\text{O}_4$ was sufficient to destroy lithium ordering in these systems. Since other trivalent cations do not show this effect at such low concentrations, it was suggested that the Mn^{+3} tend to order (or cluster) in such a way that a Jahn-Teller stabilization is made possible

via cooperative vibrational modes. This effect provides a mechanism for the local lattice inhomogeneities suggested by Bogoslovskiy, *et al.*,¹¹ as responsible for spontaneous B-H loop squareness found in magnesium-manganese ferrite.

Preliminary evidence indicated that both the iron and gallium systems exhibited anomalous increases in their lattice parameters at the critical concentration of Mn^{+3} . However, refinement of our data indicates that this is true only for the gallates. In the series $\text{Li}_{0.5}\text{Fe}_{2.5-x}\text{Mn}_x\text{O}_4$, the lattice parameters show a large dependence on the thermal history of the compounds. This effect is illustrated in Fig. V-1. Samples annealed for five days at 500°C and rapidly quenched to room temperature indicated a distinct change of symmetry at $x_c = 0.31$. This change corresponds to the loss of lithium ordering on the B-sites, and the critical concentration is indicated by the vertical line shown in the figure. This transition is not distinct in samples quenched from 800°C , and no ordering was found for those quenched from 1000°C . This result is consistent with the original work of Braun¹² on $\text{Li}_{0.5}\text{Fe}_{2.5}\text{O}_4$ and the more recent studies of Brunel and deBergevin¹³ who indicate an order-disorder transition for this material at 735°C . However, each series indicates an inflection in lattice parameter at x_c . For $x > x_c$, a linear dependence of the lattice parameters is observed for each series; for $0 < x < x_c$, a positive deviation from linearity occurs.

Fig. V-1. Compositional and temperature dependence of unit cell edges (a_0) for $\text{Li}_{0.5}\text{Fe}_{2.5-x}\text{Mn}_x\text{O}_4$ system.



Since an increase in lattice parameter is expected for increasing y in the formulation $\text{Fe}_{1-y}\text{Li}_y[\text{Li}_{0.5-y}\text{Fe}_{1.5-x+y}\text{Mn}_x^{+3}]\text{O}_4$, the divergence of the curves indicates that y is proportional both to temperature and to manganese content. The first dependence is expected from entropy considerations and the second from the relatively large preference of Mn^{+3} for octahedral sites. The independence of the inflection point on quenching temperature (and consequently on lithium ordering) and the linearity of the lattice parameters for $x > x_c$ are consistent with our previous suggestion that Mn^{+3} tends to cluster for $x > x_c$. For $x < x_c$, the Mn^{+3} ions presumably substitute randomly for Fe^{+3} .

For the gallate series, $x_c \approx 0.26$. As previously indicated, an anomalous increase in lattice parameter (apparently independent of quenching temperature) occurs at this composition. Since such an increase does not occur for the ferrite, the anomaly does not appear to be a direct

Section V

result of lost order. However, the common occurrence at x_c of both the lattice parameter discontinuity and disorder suggests that they are indirectly related. A reasonable possibility would be a discontinuity in the gallium-site-preference energy. Schulkes and Blasse¹⁴ have shown that for ordered spinels of the type $M^{+3}[\text{Li}_{0.5}M_{1.5}^{+3}]\text{O}_4$, the relative tetrahedral-site-preference energies of Fe^{+3} , Ga^{+3} , and Al^{+3} decrease in the order $\text{Ga}^{+3} > \text{Fe}^{+3} > \text{Al}^{+3}$. However, the energy terms may not be independent of ordering. For example, the tetrahedral-site preferences observed for $\text{MgM}_2^{+3}\text{O}_4$ appear to decrease in the order $\text{Fe}^{+3} > \text{Ga}^{+3} > \text{Al}^{+3}$. A discontinuity of this type would be reflected in the formulation $\text{Ga}_{1-y}\text{Li}_y[\text{Li}_{0.5-y}\text{Ga}_{1.5-x+y}\text{Mn}_x^{+3}]\text{O}_4$ as a discontinuity in y . A direct determination of y as a function of Mn^{+3} content is presently being carried out by comparison of observed and calculated x-ray intensities for lines that are largely dependent on tetrahedral-site population.

R. W. Germann
R. J. Arnott
D. B. Rogers

REFERENCES

1. A. Wold kindly supplied the samples.
2. N. Menyuk, A. Wold, D.B. Rogers and K. Dwight, J. Appl. Phys. 33, 1144S (1962).
3. N. Menyuk, A. Wold and K. Dwight, paper to be presented at Conf. on Magnetism and Magnetic Materials, 16-19 November 1964, Minneapolis, Minnesota. To be published in J. Appl. Phys. Suppl.
4. Solid State Research Report, Lincoln Laboratory, M.I.T. (1964:2), DDC 606126.
5. A. Wold (private communication).
6. Solid State Research Report, Lincoln Laboratory, M.I.T. (1964:1), DDC 601830.
7. D.B. Rogers, R.J. Arnott, A. Wold and J.B. Goodenough, J. Phys. Chem. Solids 24, 347 (1963).
8. W. Kunmann, D.B. Rogers and A. Wold, J. Phys. Chem. Solids 24, 1535 (1963).
9. H. Schafer, H. Jacob and K. Etzel, Z. anorg. Chem. 286, 27 (1956); H. Schafer, Chemische Transportreaktionen (Verlag Chemie, 1962).
10. R. Nitsche, J. Phys. Chem. Solids 17, 163 (1960); R. Nitsche, H.U. Bolsterli and M. Lichtensteiger, J. Phys. Chem. Solids 21, 199 (1961).
11. V.N. Bogoslovskiy, I. Ye. Startseva, M.G. Zhuravleva, A.A. Shchepetkin, G.I. Chufarov and Y.A. Shur, Fiz. metal. metalloved 15, 181 (1963).
12. P.B. Braun, Nature 170, 1123 (1963).
13. M. Brunel and F. deBergevin, Compt. rend. 258, 5628 (1964).
14. J.A. Schulkes and G. Blasse, J. Phys. Chem. Solids 24, 1651 (1963).

DOCUMENT CONTROL DATA - R&D

(Security classification of title, body of abstract and indexing annotation must be entered when the overall report is classified)

1. ORIGINATING ACTIVITY (Corporate author) Lincoln Labs., Lexington, Mass.		2a. REPORT SECURITY CLASSIFICATION Unclassified 2b. GROUP n/a	
3. REPORT TITLE Solid State Research			
4. DESCRIPTIVE NOTES (Type of report and inclusive dates)			
5. AUTHOR(S) (Last name, first name, initial)			
6. REPORT DATE Dec 64		7a. TOTAL NO. OF PAGES 72	
8a. CONTRACT OR GRANT NO. AF19(628)500 b. PROJECT NO. c. d.		7b. NO. OF REFS 14 8a. ORIGINATOR'S REPORT NUMBER(S) ESD-TDR-64-561 8b. OTHER REPORT NO(S) (Any other numbers that may be assigned this report)	
10. AVAILABILITY/LIMITATION NOTICES Qualified requesters may obtain from DDC. Aval from OTS.			
11. SUPPLEMENTARY NOTES		12. SPONSORING MILITARY ACTIVITY ESD, L G Hanscom Field, Bedford, Mass.	
13. ABSTRACT This report covers in detail the solid state research work at Lincoln Laboratory for the period 1 July 1964 through 30 September 1964. The topics covered are Solid State Device Research, Laser Research, Materials Research, Band Structure and Spectroscopy of Solids, and Magnetism and Resonance.			

14.

KEY WORDS

LINK A

LINK B

LINK C

ROLE

WT

ROLE

WT

ROLE

WT

Solid State
Laser
Band Structure
Magnetism
Resonance

INSTRUCTIONS

1. **ORIGINATING ACTIVITY:** Enter the name and address of the contractor, subcontractor, grantee, Department of Defense activity or other organization (corporate author) issuing the report.

2a. **REPORT SECURITY CLASSIFICATION:** Enter the overall security classification of the report. Indicate whether "Restricted Data" is included. Marking is to be in accordance with appropriate security regulations.

2b. **GROUP:** Automatic downgrading is specified in DoD Directive 5200.10 and Armed Forces Industrial Manual. Enter the group number. Also, when applicable, show that optional markings have been used for Group 3 and Group 4 as authorized.

3. **REPORT TITLE:** Enter the complete report title in all capital letters. Titles in all cases should be unclassified. If a meaningful title cannot be selected without classification, show title classification in all capitals in parentheses immediately following the title.

4. **DESCRIPTIVE NOTES:** If appropriate, enter the type of report, e.g., interim, progress, summary, annual, or final. Give the inclusive dates when a specific reporting period is covered.

5. **AUTHOR(S):** Enter the name(s) of author(s) as shown on or in the report. Enter last name, first name, middle initial. If military, show rank and branch of service. The name of the principal author is an absolute minimum requirement.

6. **REPORT DATE:** Enter the date of the report as day, month, year; or month, year. If more than one date appears on the report, use date of publication.

7a. **TOTAL NUMBER OF PAGES:** The total page count should follow normal pagination procedures, i.e., enter the number of pages containing information.

7b. **NUMBER OF REFERENCES:** Enter the total number of references cited in the report.

8a. **CONTRACT OR GRANT NUMBER:** If appropriate, enter the applicable number of the contract or grant under which the report was written.

8b, 8c, & 8d. **PROJECT NUMBER:** Enter the appropriate military department identification, such as project number, subproject number, system numbers, task number, etc.

9a. **ORIGINATOR'S REPORT NUMBER(S):** Enter the official report number by which the document will be identified and controlled by the originating activity. This number must be unique to this report.

9b. **OTHER REPORT NUMBER(S):** If the report has been assigned any other report numbers (either by the originator or by the sponsor), also enter this number(s).

10. **AVAILABILITY/LIMITATION NOTICES:** Enter any limitations on further dissemination of the report, other than those

imposed by security classification, using standard statements such as:

- (1) "Qualified requesters may obtain copies of this report from DDC."
- (2) "Foreign announcement and dissemination of this report by DDC is not authorized."
- (3) "U. S. Government agencies may obtain copies of this report directly from DDC. Other qualified DDC users shall request through _____."
- (4) "U. S. military agencies may obtain copies of this report directly from DDC. Other qualified users shall request through _____."
- (5) "All distribution of this report is controlled. Qualified DDC users shall request through _____."

If the report has been furnished to the Office of Technical Services, Department of Commerce, for sale to the public, indicate this fact and enter the price, if known.

11. **SUPPLEMENTARY NOTES:** Use for additional explanatory notes.

12. **SPONSORING MILITARY ACTIVITY:** Enter the name of the departmental project office or laboratory sponsoring (paying for) the research and development. Include address.

13. **ABSTRACT:** Enter an abstract giving a brief and factual summary of the document indicative of the report, even though it may also appear elsewhere in the body of the technical report. If additional space is required, a continuation sheet shall be attached.

It is highly desirable that the abstract of classified reports be unclassified. Each paragraph of the abstract shall end with an indication of the military security classification of the information in the paragraph, represented as (TS), (S), (C), or (U).

There is no limitation on the length of the abstract. However, the suggested length is from 150 to 225 words.

14. **KEY WORDS:** Key words are technically meaningful terms or short phrases that characterize a report and may be used as index entries for cataloging the report. Key words must be selected so that no security classification is required. Identifiers, such as equipment model designation, trade name, military project code name, geographic location, may be used as key words but will be followed by an indication of technical context. The assignment of links, rules, and weights is optional.